

FRACTURE STRENGTH OF THE
SIC LAYER IN TRISO COATED
FUEL PARTICLES

by

Brian Campbell Davis

© Copyright by Brian Campbell Davis, 2013

All Rights Reserved

A thesis submitted to the Faculty and the Board of Trustees of the Colorado School of Mines in partial fulfillment of the requirements for the degree of Master of Science (Mechanical Engineering).

Golden, Colorado

Date _____

Signed: _____

Brian Campbell Davis

Signed: _____

Dr. Ivar Reimanis
Thesis Advisor

Signed: _____

Dr. John Berger
Thesis Advisor

Golden, Colorado

Date _____

Signed: _____

Dr. John Berger
Interim Department Head
Department of Mechanical Engineering

ABSTRACT

The SiC layer in the TRISO coating of next generation nuclear fuel particles is a structural element which ensures the containment of fissile products, thus forming the basis of the safety rationale for the reactor. Due to the inherent variability in ceramics, which can be affected by different manufacturing methods, application substrates, and geometries; it is important to characterize the fracture strength of this application specific ceramic. Hence, diametrical compression tests were performed on a sample population of SiC hemispheres, which were made from actual TRISO coatings. Multiple numerical analysis methods were used to design the test, understand the mechanics involved, and ultimately determine values for fracture strength. For an initial sample population of 8 hemispheres, the characteristic strength and Weibull modulus were 487 MPa and 4.0, respectively. Sensitivity analyses revealed that divot radius is the most important variable, followed by shell thickness and outside radius. The additional holistic results of this research are theoretical and experimental methodology improvements which constitute a value added step forward in destructive TRISO coated nuclear fuel particle testing.

TABLE OF CONTENTS

ABSTRACT	iii
LIST OF FIGURES	viii
LIST OF TABLES	x
LIST OF SYMBOLS	xii
LIST OF ABBREVIATIONS	xvi
ACKNOWLEDGMENTS	xviii
DEDICATION	xix
CHAPTER 1 INTRODUCTION	1
1.1 Umbrella Project	1
1.2 TRISO Coated Fuel Particle	2
1.3 SiC Shell	3
1.4 Problem Statement: Fracture Strength	3
1.5 Extending Current Research	4
1.6 Rationalization of Experiments	4
CHAPTER 2 LITERATURE REVIEW	6
2.1 SiC Shell Material Properties	6
2.2 Crush Plate Characterization	7
2.3 Isolated SiC Shell Mechanical Testing	7
2.3.1 Brittle Ring Tests (O-ring and C-ring)	8
2.3.2 Internal Pressurization Tests	8

2.3.3	Hemisphere Bending Tests	9
2.3.4	Diametrical Compression Tests	11
2.3.5	Summary of Previous Research Results	14
2.3.6	Summary of Previous Research Conclusions	15
CHAPTER 3 METHODOLOGY		17
3.1	TRISO Coated Particle Manufacturing	17
3.2	Test Article Preparation	17
3.2.1	Equipment List	17
3.2.2	Procedure	18
3.3	Radio Microscopy Measurement and Inspection	19
3.3.1	Equipment List	20
3.3.2	Procedure	20
3.3.3	Geometric Calculations	21
3.3.4	Limitations and Systematic Errors	24
3.4	Load Cell Crush Tests	25
3.4.1	Equipment List	25
3.4.2	Procedure	26
3.5	Post-Test Measurement and Inspection	27
3.5.1	Equipment List	27
3.5.2	Procedure	27
3.6	Numerical Analysis	28
3.6.1	Analytic Solution	31
3.6.1.1	Linearly Interpolated Curve	33

3.6.1.2	Error Analysis	34
3.6.1.3	Sensitivity Analysis	37
3.6.1.4	Divot Asphericity	38
3.6.2	3D Finite Element Analysis	38
3.6.2.1	Material Properties	40
3.6.2.2	Convergence Studies	42
3.6.2.3	Accurate Divot Size	44
3.6.2.4	Linearly Interpolated Curve	45
3.6.2.5	Error and Sensitivity Analysis	46
3.6.2.6	Shell Stress Distribution	46
3.6.3	Weibull Distribution Calculations	47
CHAPTER 4	RESULTS AND DISCUSSION	52
4.1	Primary Test Article Failure Mechanism	52
4.2	3D Finite Element Analysis Convergence Study	53
4.3	Test and Analysis Characterization	57
4.3.1	Empirical Average Geometry Data	57
4.3.2	Initial Analytic Solution Linearly Interpolated Curves	58
4.3.3	FEA Solution Linearly Interpolated Curves	59
4.3.4	Multiple Solution Linearly Interpolated Curves	60
4.3.5	Maximum Principal Stress Profile on Inner Shell Surface	62
4.3.6	Critical Maximum Principal Stress	64
4.4	Error and Sensitivity Characterization	65
4.4.1	Analytic Solution Quantitative Error	66

4.4.2	Analytic Solution Input Variable Sensitivity	67
4.4.3	FEA Error and Sensitivity	70
4.5	Discrete Empirical Data Points	70
4.5.1	Analytic Solution with Error Propagation	71
4.5.2	FEA Model Solution for Supremum Principal Stress	73
4.5.3	FEA Model Solution for Stress Profile	75
4.5.4	Iterative Weibull Distribution and Characteristic Strength	77
4.5.5	Divot Size and Asphericity	79
4.5.6	Multi-Method Conservative Weibull Distribution	81
CHAPTER 5 CONCLUSIONS		83
REFERENCES CITED		86
APPENDIX - SELECT ANALYSIS RESULTS IN TABULAR FORM		89

LIST OF FIGURES

Figure 1.1	Diagram of TRISO Coating Layers around a Nuclear Fuel Sphere	2
Figure 2.1	Diagram of Previous Hemisphere Bending Tests	10
Figure 2.2	Principal Stresses on Inner Wall of SiC Hemispherical Shell	12
Figure 3.1	Difference Between Measured and Actual Diameter	22
Figure 3.2	Qualitative Example SEM Image of Test Article Asphericity	25
Figure 3.3	Process Flow Diagram for Analytic Solution Methods	29
Figure 3.4	Process Flow Diagram for all Experimental Data Solution Methods	30
Figure 3.5	Diagram for Analytic Solution Scenario	31
Figure 3.6	Screenshot of FEA Model and Element Discretization	39
Figure 3.7	Sample Indenter Material Curve with 4 Distinct Sections	41
Figure 3.8	Circumferential FEA Results Path on Inner Surface of Shell	47
Figure 4.1	SiC Shell Piece Created by Fracture Initiation near Hemisphere Apex	52
Figure 4.2	FEA Convergence with Changes in Shell Discretization	53
Figure 4.3	FEA Convergence with Changes in Indenter Discretization	54
Figure 4.4	Main FEA Convergence Study	55
Figure 4.5	Exaggerated Deformed Shape of “05” Convergence Study Model	56
Figure 4.6	Stress vs. Load and Divot Size for the Analytic Solution	58
Figure 4.7	Analytic Solution σ_t vs. P for Different BHN Materials (Reference Only)	59
Figure 4.8	FEA Data Points and Power Law Curve Fit for r_d vs. F_R	60
Figure 4.9	FEA and Analytic Solution Linearly Interpolated Stress vs. Force	61

Figure 4.10	Maximum Principal Stress (σ_{p1}) Profile for Multiple Divot Sizes	62
Figure 4.11	Principal Stresses ($\sigma_{p1}, \sigma_{p2}, \sigma_{p3}$) Profile (Reference Only)	63
Figure 4.12	Maximum Principal Stress (σ_{p1}) Profile Under Divot Area	64
Figure 4.13	Analytic Solution Sensitivity Levels from AMV+ Method	69
Figure 4.14	FEA Model Sensitivity Levels from AMV+ Method	70
Figure 4.15	Results of Pseudo-Hardness Test on Crush Plate Material	71
Figure 4.16	Analytic Solution with Error Bars for Empirical Data Points	72
Figure 4.17	FEA Model σ_{pS} vs. F_R Empirical Data Points	75
Figure 4.18	FEA Model Stress Profile on Inner Surface of SiC Shell	76
Figure 4.19	Typical Brass (left) and Nickel (right) Divot Marks under SEM	79
Figure 4.20	Stress (σ_t) vs. Dimensionless Divot Asphericity (r_{0asp})	80

LIST OF TABLES

Table 2.1	Detailed Results from Hemispherical Bending	10
Table 2.2	Summary of Strengths for Isolated CVD SiC Particle Material	14
Table 4.1	Selected Main FEA Convergence Study Configuration Results	56
Table 4.2	Test Characterization Input Data (Average Geometry)	57
Table 4.3	Min. & Max. Stress Profile Values Under Divot	65
Table 4.4	Monte Carlo Error Analysis Convergence Study	66
Table 4.5	Comparison of Different Error Propagation Techniques ($\delta r_0 = 5\%$)	67
Table 4.6	Sensitivity of Analytic Solution Error to Input Errors	68
Table 4.7	Sensitivity of Analytic Solution to Input Values	68
Table 4.8	Input Data to Preliminary Weibull Distribution	72
Table 4.9	Results From Preliminary Weibull Distribution	73
Table 4.10	Analytic Solution & FEA Model: Stress, Force, and Divot Size	74
Table 4.11	FEA Model Stress Profile Numerical Data	76
Table 4.12	Results From Iterative Method Weibull Distribution	77
Table 4.13	Fracture Strength for High and Low Asphericity Divot Sizes	80
Table 4.14	Fracture Strength for High and Low Asphericity Divot Sizes	81
Table A.1	FEA Intermediate Convergence Studies	90
Table A.2	FEA Main Convergence Study	91
Table A.3	FEA Model Linearly Interpolated Solution	92
Table A.4	Analytic Solution with Error for Empirical Data	92

Table A.5 Empirical Input Data (with Height-Corrected Geometry) 93

LIST OF SYMBOLS

Young's Modulus	E
Maximum Young's Modulus	E_0
Young's Modulus Formula Constant (3.57)	C
SiC Porosity	V_P
Poisson's Ratio	ν
Inside Radius of SiC Shell	r_i
Minimum Measured Shell Outside Radius	R_{Mmin}
Average Measured Shell Outside Radius	R_{Mav}
Maximum Measured Shell Outside Radius	R_{Mmax}
Hemisphere Height	h
Nominal Shell Outside Radius	R
Variable Error	δ
Sample Index	i
Number of Samples	N
Indexed Sample Value	x_i
Mean of Sample Set	\bar{x}
Standard Deviation of Sample Set	\bar{S}
Mean of Measured Shell Thicknesses (One Shell)	\bar{t}_M
Shell Thickness	t
Intermediate Analytic Solution Variable	μ

Intermediate Analytic Solution Coefficient #1	C_1
Intermediate Analytic Solution Coefficient #2	C_2
Radius of Distributed Pressure Acting on Shell	r_0
Shell Outside Radius	R_2
Resultant Force Acting on Shell	P
Shell Angular Depth	ϕ
Membrane Stress	$\sigma_{membrane}$
Bending Stress	$\sigma_{bending}$
Total Stress	σ_t
Intermediate Analytic Solution Error Analysis Variable	η
Force Increment for Linearly Interpolated Curve	ΔP
Power Law Curve Fit Coefficient Constant	K
Power Law Curve Fit Power Constant	n
Minimum Radius of Divot	r_{min}
Average Radius of Divot	r_{av}
Maximum Radius of Divot	r_{max}
Dimensionless Divot Asphericity	r_{asp}
Plastic Stress	σ_p
Plastic Strain	ϵ_p
First Point in Plastic Stress vs. Plastic Strain Curve	σ_{p1}
First Point in Plastic Stress vs. Plastic Strain Curve	ϵ_{p1}
Indexed Point in Plastic Stress vs. Plastic Strain Curve	σ_{pi}
Indexed Point in Plastic Stress vs. Plastic Strain Curve	ϵ_{pi}

Final Point in Plastic Stress vs. Plastic Strain Curve	σ_{pf}
Final Point in Plastic Stress vs. Plastic Strain Curve	ϵ_{pf}
Theoretical Divot Depth	l_{td}
Prescribed Divot Depth	l_{pd}
Divot Depth Adjustment Constant	C_{adj}
Divot Radius	r_d
Reaction Force	F_R
Supremum Principal Stress in the Shell	σ_{pS}
Weibull Distribution Random Variable	x
Weibull Distribution Scale Parameter	λ
Weibull Distribution Shape Parameter	k
Fracture Stress	σ_f
Characteristic Strength	σ_0
Weibull Modulus	m
Probability of Failure at Fracture Stress	P_f
Probability of Failure at Indexed Stress Value	P_i
Characteristic Strength of Local Area	σ_0^L
Characteristic Strength of Full Shell	σ_0^F
Local Surface Area	S_E^L
Full Shell Surface Area	S_E^F
Average Radius of Distributed Pressure Acting on Shell	\bar{r}_0
Average Shell Outside Radius	\bar{R}_2
Average Shell Thickness	\bar{t}

Indexed Fracture Strength in Local Area	σ_{fi}^L
Indexed Fracture Strength in Full Shell	σ_{fi}^F
Indexed Radius of Distributed Pressure Acting on Shell	\bar{r}_0
Iterative Solution Convergence Tolerance	ϵ
Max. Principal Stress	σ_1
Mid. Principal Stress	σ_2
Min. Principal Stress	σ_3
FEA Global Coordinate System Y-axis Postion	y
Number of Test Articles	N
Radius at 90% Supremum Principal Stress	$r_{90\%}$

LIST OF ABBREVIATIONS

Advance Mean Value Plus Iterations	AMV+
Brinell Hardness Number	BHN
Buffered Oxide Etchant	BOE
Carbon Monoxide	CO
Colorado Center for Advanced Ceramics	CCAC
Colorado School of Mines	CSM
Comma Delimited Data File	CSV
Cumulative Distribution Function	CDF
Deionized	DI
Department of Energy	DOE
Finite Element Analysis	FEA
Finite Element Method	FEM
Graphical User Interface	GUI
High Temperature Gas Reactor	HTGR
Idaho National Laboratory	INL
Inner Pyrolytic Carbon	IPyC
Light Water Reactor	LWR
Next Generation Nuclear Plant	NGNP
Nuclear Regulatory Commission	NRC
Outer Pyrolytic Carbon	OPyC

Partial Differential Equation	PDE
Pyrolytic Carbon	PyC
Scanning Electron Microscope	SEM
Silicon Carbide	SiC
Tri-Isotropic	TRISO
United Kingdom	UK
Very High Temperature Reactor	VHTR
Zirconium dioxide	ZrO ₂

ACKNOWLEDGMENTS

The author would like to acknowledge numerous organizations for their assistance: The United States Department of Energy (DOE), for the funding and leadership that made this portion of Next Generation Nuclear Plant (NGNP) research possible along with nearly all recent research referenced herein. Materials Science and Technology Division of Oak Ridge National Laboratory (ORNL), for previous groundwork research and additional guidance on the diametrical compression of TRISO SiC shells. Colorado School of Mines (CSM), for the overall educational and institutional environment that made this work possible along with furthering the author's education with additional high-level engineering skill sets. Colorado Center for Advanced Ceramics (CCAC), for the labs, equipment, human resources, and organizational structure that make this ceramic-specific nuclear energy research possible. Campus Computing, Communications and Information Technologies (CCIT), for the computational infrastructure (including multiple supercomputers) and software license management that makes possible all of the numerical analysis performed in this research.

The author would also like to acknowledge numerous individuals for their assistance: Dr. Ivar Reimanis, for overseeing and guiding this research on a daily basis, ultimately ensuring success of the overall research project. Brent Fillery, for authoring the original Abaqus python script and providing significant assistance in conducting Abaqus FEA simulations. Dr. Brian Gorman, for general guidance in the conduction of this research at CCAC. Dr. Darryl P. Butt and Dr. John Youngsman, for procedure development and conduction of test article preparation. Dr. John Berger, for guidance in general solid mechanics and conduction of mechanical engineering research. Dr. Anthony Petrella, for assistance in the practical application of Abaqus FEA and NESSUS statistical software. Dr. Panos Kiouisis, for assistance in understanding theory behind the Finite Element Method (FEM). Dr. Timothy Kaiser, for assistance in using Abaqus FEA on the CSM supercomputer, "Ra".

This work is dedicated to any individual who finds it useful in their pursuit of science and engineering.

“We must never forget that the scientific and technical accomplishments of today are not the exclusive products of this generation. They are the results of the labors and the thoughts of countless individuals over the centuries. They are the sum and substance of that continuous wave of progress to which each generation has made its contribution. Thus, it is incumbent on us not only to safeguard this precious heritage - one of the highest expressions of man’s unselfish achievement - but to enrich it with our own particular contribution and ensure its transference to our successors.”

- John J. Hopkins -

CHAPTER 1

INTRODUCTION

The research in this thesis is funded by the Department of Energy (DOE) as part of their development effort to realize new commercially viable nuclear reactor designs for use in the USA and export. As is common in such projects; acronyms, funding intermediaries, and sub-project naming conventions can become difficult to follow as they involve multiple agencies, laboratories, organizations, and commercial partners. This chapter contains a simplified explanation of the overall DOE project and the specific research being conducted by the Colorado Center for Advanced Ceramics (CCAC) at the Colorado School of Mines (CSM).

1.1 Umbrella Project

The initialization of the top-level project, the Next Generation Nuclear Plant (NGNP), is summarized in a status report from the Idaho National Laboratory (INL):

The Next Generation Nuclear Plant (NGNP) Project was established based on a Department of Energy (DOE) Generation IV Research and Development (R&D) evaluation completed in 2003 to integrate high-temperature reactor technology with advanced hydrogen, electricity, and process heat production capabilities. The project was authorized via the Energy Policy Act of 2005 (EPAAct).[1]

Several Generation IV nuclear reactors were being considered for the NGNP and the final design chosen was the Very High Temperature Reactor (VHTR). While it is unclear if it is a synonym or a subset of the VHTR, most documentation available labels the NGNP reactor of choice as the High Temperature Gas Reactor (HTGR). The economic and environmental benefits of the HTGR are outlined in the following excerpt from another INL publication:

Because the HTGR is helium cooled with a graphite core it can operate at reactor outlet temperatures much higher than conventional LWR technology.

Accordingly, HTGRs can be used in place of fossil fuels in industrial applications and for generation of electric power, reducing or eliminating the greenhouse gas (GHG) emissions from these fuels. The use of the HTGR also provides a long term secure energy source at a stable price insulating the end user from the economic uncertainties associated with the volatility in the price and availability of fossil fuels.[2]

From a technical standpoint, an HTGR is a helium-cooled graphite-moderated nuclear reactor that operates between 700 °C and 950 °C. While there are two different core designs (prismatic and pebble bed) both of them rely on the same nuclear fuel particles. These particles feature a ceramic coating and are therefore extremely robust, being able to retain fissile materials under extreme conditions. Because the particles are essentially spherical, their coating is referred to as tri-isotropic (TRISO).

1.2 TRISO Coated Fuel Particle

The TRISO coated fuel particle, pictured in Figure 1.1, is the NGNP HTGR fuel of choice. While other aspects of the HTGR are still being decided, it is apparent that this will be the nuclear fuel used.[2]

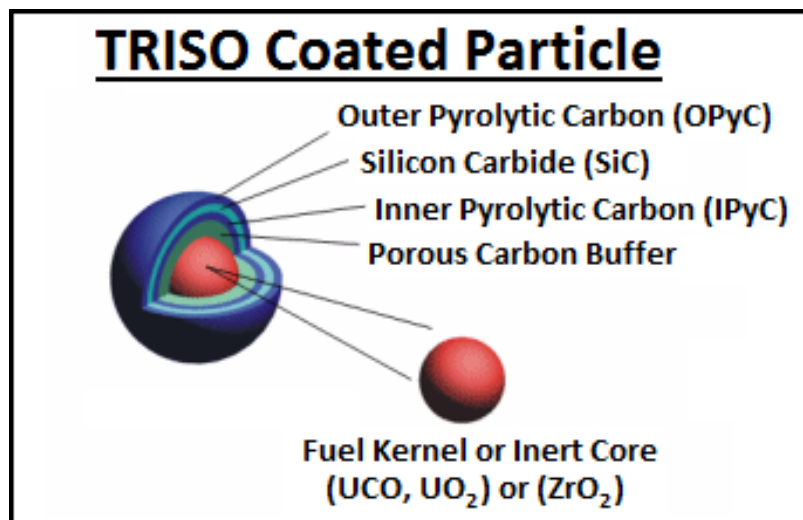


Figure 1.1: Diagram of TRISO Coating Layers around a Nuclear Fuel Sphere

What separates this fuel from current Light Water Reactor (LWR) nuclear fuels are the layers encasing the fissile material. The silicon carbide (SiC) ceramic layer has a structural functionality which ensures there is no unintended release of fissile materials and most importantly, the particle cannot melt. The SiC layer is at the heart of the rationale for the inherent safety of the NGNP and it is extremely important in the final decision making process which will allow the HTGR to be licensed by the Nuclear Regulatory Commission (NRC). [3] (Licensing is a necessary step in reaching the final goal of developing commercial installations.)

1.3 SiC Shell

The process of manufacturing a TRISO coated fuel particle starts with a uranium oxide (UO_2) sphere. In separate process steps, each coating layer is applied to the sphere. The SiC layer is applied using Chemical Vapor Deposition (CVD). This ensures a high purity layer of SiC with few flaws and a relatively even thickness. In general, the post-application mechanical properties of a ceramic CVD layer are highly dependent on the texture of the base it is applied to, along with numerous other process parameters. Thus, the material properties of the SiC layer in the TRISO coated fuel particle cannot be assumed to be inherently similar to CVD SiC in other shapes, applications, or processes. The TRISO coating SiC layer must be scrutinized as a unique material, especially considering its role as a safety feature for preventing the release of dangerous fissile materials into the environment.

1.4 Problem Statement: Fracture Strength

SiC exhibits brittle fracture, wherein the material has a linear stress strain curve until the ultimate tensile strength is reached and it fails by way of a crack(s) propagating through the material. (Note: In brittle fracture, ultimate tensile strength is regularly referred to as fracture strength.) In the case of the TRISO coated fuel particle, the particle can contain the bulk of the fissile material so long as the SiC shell remains intact and no crack penetrates the full thickness of the spherical shell. Thus, if the TRISO coated fuel particle reaches a

stress state where the ultimate tensile strength of the SiC layer is surpassed, that structural shell will fracture and dangerous fissile materials will be released. It is for this reason that understanding the fracture strength of this application-specific CVD SiC shell is so important.

1.5 Extending Current Research

The work performed at CCAC is not the first time a research group has investigated the fracture strength of the SiC layer of a TRISO coated fuel particle. Several other groups have worked on this in the past, including researchers at the Oak Ridge National Laboratory (ORNL) and the South Korean Department of Nuclear Engineering. However, due to the small size and complex shape of the shell, each set of experiments raises concerns to the accuracy of the results. The research contained in this document does not seek to disprove or discredit any previous research on the subject. Rather, it seeks to: take into consideration the lessons learned from previous research, reduce the experimental limitations of those efforts by using a more thorough and exhaustive approach, and contribute new results and conclusions that have a significant value added in attaining the overall goal of fully understanding the failure mechanisms of the SiC layer in TRISO coated fuel particles.

1.6 Rationalization of Experiments

The research performed at CCAC is the result of a well thought-out process in which previous research was taken into consideration and specific research activities were evaluated and approved based on their apparent value added to the overall DOE effort to better characterize the fracture strength of the TRISO coated particle's SiC layer. The following list makes up the experimental and theoretical activities performed as part of this research:

- Experimental Laboratory Work
 - Crush Plate Material Property Characterization
 - Individual Test Article Geometry Measurement

- Diametrical Compression Crush Testing
- Post-Fracture Test Article Inspection
- Theoretical Numerical Analysis
 - Partial Differential Equation (PDE) Analytic Solution
 - * Deterministic Maximum Principal Stress at Apex
 - * Error Propagation (Monte Carlo, AMV+, Delta Method)
 - * Input Variable Sensitivity Analysis
 - * Divot Asphericity Correlation to Results
 - 3D Finite Element Analysis (FEA) Solution
 - * Supremum Principal Stress in Test Article
 - * Error Propagation Through AMV+ Method
 - * Stress Profile on Inner Surface of Test Article
 - Weibull Distribution Statistical Analysis
 - * Distribution Parameters with Constant Area
 - * Iterative Solution for Varying Surface Area

Each activity involves some form of new, value-added components not part of previous research efforts. Concerning the reporting of this research, significant efforts were made to communicate information so that other DOE funded researchers can easily understand the work performed herein and build upon it in the future.

CHAPTER 2

LITERATURE REVIEW

The TRISO coated nuclear fuel particle was initially developed in Europe, with the first large group of publications being made in the early 1970s. Since then, there have been research efforts in different nations and the particle's overall proliferation has resulted in a wealth of published data. The specific information desired in this literature review pertains to previous efforts in understanding the fracture strength of the SiC layer in the TRISO coating. Additionally, due to required input values for numerical solutions, the results of research work pertaining to Young's modulus, Poisson's ratio, and other material properties are also sought.

2.1 SiC Shell Material Properties

Sometimes separate from the fracture strength data are previous research efforts to determine Young's modulus and Poisson's ratio for the SiC layer of a TRISO coating. As the work herein is not interested in creating new data for these values, the literature review is limited to finding acceptable values. Fortunately, a good summary for these experimental values has already been published by researchers at ORNL [4]. The formula for Young's Modulus is shown in Equation 2.1.

$$E = E_0 \exp(-CV_p) \tag{2.1}$$

Where:

E = Young's Modulus

E_0 = Maximum Young's Modulus = 460 GPa

C = Constant = 3.57

V_p = Porosity

Additionally, the publication states that Young's modulus (i.e. Elastic modulus) has an uncertainty of $\pm 10\%$ for low porosity SiC ($V_p < 1\%$) and $\pm 15\%$ at higher porosities [4]. The Young's modulus used in the most recent diametrical compression tests is $E = 450\text{GPa}$ [5].

The selection of a Poisson's ratio to use in calculations is much easier to reach. It is summarized in the following excerpt:

...the highest value of 0.21 was typically obtained for pure CVD SiC, which best represents the TRISO fuel material... ...temperature dependence on the Poisson's ratio is at best very minor... ...Poisson's ratio of SiC is therefore assumed to be a constant (~ 0.21)... [4]

Thus, the values of $E = 450\text{GPa}$ and $\nu = 0.21$ will be used for all numerical analysis contained herein.

2.2 Crush Plate Characterization

While it is not necessary for the analytic solution, the FEA solution requires mechanical properties for the crush plate. Specifically, it requires Poisson's ratio, Young's modulus, and a true stress vs. true strain curve expressed as true stress vs. true plastic strain. Poisson's ratio for brass 260 ($\nu = 0.375$) was found at a reliable website [6]. The experimental generation of true stress vs. true strain, along with Young's modulus, will be done in accordance with an internal procedure at CSM.

2.3 Isolated SiC Shell Mechanical Testing

There have been many previous research efforts focused on the mechanical testing of the SiC layer of TRISO coatings. In each of these tests, a portion of the SiC layer is isolated from the other layers through multiple process stages (e.g. grinding, polishing, burning off PyC layers). These previous efforts are reviewed in the most detail, due to their direct relation to the research being performed herein.

2.3.1 Brittle Ring Tests (O-ring and C-ring)

One of the first published mechanical tests of the SiC layer (referred to as “HTR particle coatings” at the time) was performed by K. Bongartz et al. in Germany in 1972 [7]. In this initial research, one of the key goals was to experiment on actual fuel particle material, not SiC that had been deposited on other geometries. In summary, material from opposing sides of the sphere were removed in order to create a near cylindrical ring of SiC at the equator. This ring was placed vertically in a crush test loading fixture with sapphire plates. The equations used to calculate Young’s modulus and fracture stress were taken from the work of S. Timoschenko [8]. (Revisiting this test again in a longer 1976 publication, K. Bongartz et al. applied Weibull statistical analysis to their results [9]). One key point noted in the first paper is the wide distribution in results (standard deviation is 21–23% [7])

The brittle ring test was later used by Japanese researchers K. Minato et al. in 1982 on samples that had undergone different doses of irradiation [10]. The ring test was again employed by S.J. Xu et al. in 1995 to determine the effect of deposition temperature on the SiC layer of TRISO particles for a Chinese 10 MW research reactor [11]. The resulting values from these two studies are very different (Table 2.2). Due to the different national origin and lack of transparency into every detail in the testing process, it is uncertain what caused this. However, one must first look to the assumed different manufacturing origins of the TRISO particles to explain the discrepancy in results.

2.3.2 Internal Pressurization Tests

In 1972, K.E. Gilchrist et al. in the UK published a short paper on measuring the strength of the SiC solely by internal pressurization of a hemisphere [12]. This first attempt highlighted the tedious nature of performing this type of test on a population of 66 isolated SiC shells; however, it also emphasized that this test best represents the in-service stresses, where particles are expected to fail from internal pressurization caused by buildup of fission-product gases. The final results of this test (fracture strengths ~ 100 MPa) were concluded

to be comparable with other mechanical testing results of the time. These results should not be directly compared to modern tests because of dimensional differences (e.g. inner radius of the SiC shells was 1mm, considerably larger than modern samples).

The internal pressurization test was later performed by S. G. Hong et al. at ORNL and published in 2007 [13]. It is also published in a less prolific set of conference proceedings [14]. In their testing, the sample was ground and polished below the equator, thus ensuring there was still a full hemisphere free from being constrained by epoxy. A total of 32 samples were tested with internal pressurization and the data produced matched general ranges for SiC. However, in their Weibull statistical calculations they state that two orthogonal hoop stresses results in the effective surface area being $4\pi r_i^2$, thus doubling the actual surface area. The inner surface area of a hemisphere is $2\pi r_i^2$, but this does not simply double with the stress condition. When an equibiaxial stress condition is expressed in three dimensions, it does have two axes that are equal. However, the equibiaxial stress can also be visualized as a planar hydrostatic stress, where stress is equal in all directions in the tangential plane. Thus, a stress pattern multiplier of 2 is more of an artifact of a three dimensional coordinate system than an accurate compensation for the actual stress condition. The importance of the equibiaxial stress pattern will be further addressed in the work herein.

2.3.3 Hemisphere Bending Tests

Also in the group of early TRISO coating researchers, A.G. Evans et al. in the UK published their work on SiC strength in 1973 [15]. This was the first work involving a flexural test and two different tests were performed to flex the outer or inner surface of the shell. Diagrams of these tests are shown in Figure 2.1.

Being the first tests of this kind, larger scale models of aluminum oxide and glass with strain gauges attached were also tested, in order to calibrate constants in the numerical analysis. This type of test was repeated again in 1976 by A. Briggs et al., a research group with some of the same members [16]. In this second round of testing, experiments on aluminum oxide and glass models were re-performed in order to attain more accurately calibrated

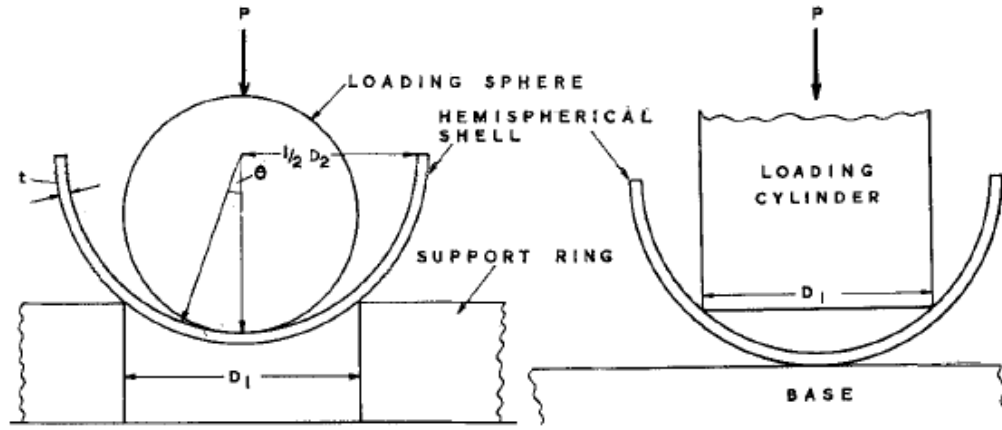


Figure 2.1: Diagram of Previous Hemisphere Bending Tests [15]

constants. When looking at the reprinting of these research results in row 6 of Table 2.2, it is important to understand that the wide range in characteristic strength is misleading. That range encompasses two different tests (inner surface and outer surface). If we consider that failure occurs after a surface flaw initiates a crack, then we can understand that testing different surfaces is essentially testing different materials, especially if the surface roughness is different, which it typically is. Table 2.1 contains the results of the original paper, which show two different sets of more precise results.

Table 2.1: Detailed Results from Hemispherical Bending [16]

Batch no.	Inner Surface Strength		Outer Surface Strength	
	Mean (MN/m ²)	Weibull modulus	Mean (MN/m ²)	Weibull modulus
ACR 1424	3170	7.8	1910	8.4
ACR 1467	2950	6.6	1870	7.2

One lesson learned is that although summaries like Table 2.2 are convenient and useful, the original publications must be reviewed in order to prevent misunderstandings about the original data's true nature. Furthermore, the research contained herein is only focused on strength values determined from stressing the inner surface because this is the expected crack initiation surface for in-service conditions.

2.3.4 Diametrical Compression Tests

Unlike other testing methods first published in the early 1970s, diametrical compression testing is a more recent development. This test is reviewed in more depth, because diametrical compression tests make up the experimental portion of the research contained herein. This method has been significantly advanced by researchers at ORNL. In particular, there are two sets of experiments which have yielded a wealth of information about the solid mechanics and general characteristics of the test.

The first diametrical compression experiment is published in two documents previously cited herein for the internal pressurization experiments they also contain [13][14]. The most important aspect to note is that the crush plate is made of tool steel, a relatively hard material compared to later implementations of this test. This results in a very small contact area between the crush plate and SiC shell. Overall, the stress concentration in the shell was found to be “...highly localized at the inner surface just beneath the loading contact region...”[13]. Additionally, the importance of quantifying the contact area by measuring the divot in the crush plate material is mentioned in different sections of the publication:

...results reveal that the fracture strengths of both materials significantly depend on the initial contact area... ...the proper value for contact area should be defined through experimental observation. [13]

In addition to contact area, the publication also highlights the Weibull modulus (m) as highly influential in the strength scaling relationship which calculates the final predicted strength of an entire shell. Thus, it emphasizes the importance of obtaining a value for m which is reliable.

Most importantly, this publication contains valuable data concerning stress distribution on the inner surface of the shell (Figure 2.2). First, the critical stress state is established in 3D as having two orthogonal tensile hoop stresses on the inner surface and a radial compression component. The radial compression is ignored because it does not affect fracture strength.

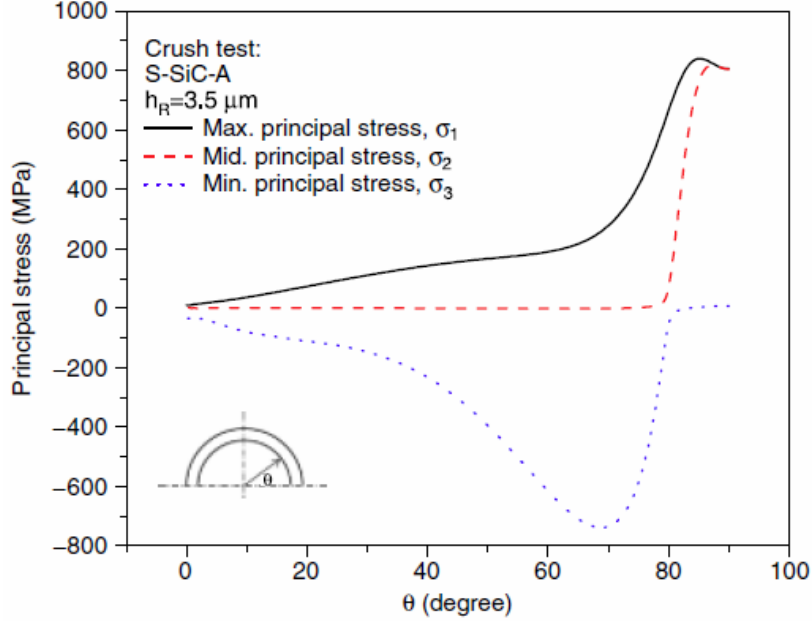


Figure 2.2: Principal Stresses on Inner Wall of SiC Hemispherical Shell [13]

The two tensile hoop stresses are equal close to 90° , which is the apex of the hemisphere. This represents equibiaxial stress, where the stress is equal in all directions on the tangential plane. However, for a 3D coordinate system it is represented by two equal max. principal stresses. What is most insightful is that as the position angle reduces ($\sim 85^\circ$) the two stresses become unequal, establishing one as max. principal and the other as mid. principal. Furthermore, at this location the max. principal stress is larger than at the apex. This means that an analytic solution which solves for the max. principal stress at the apex of the shell does not always solve for the maximum max. principal stress of the whole shell, the supremum principal stress (σ_{pS}), because that value is located adjacent to the apex. From this, one would expect the fracture to initiate near the apex, but not exactly at the apex.

The next diametrical compression test is also published in two documents by the Materials Science & Technology Division of ORNL [5][17]. These documents describe tests which use a piece of brass foil as the crush plate. This is nearly identical to the experiments contained in the present research. One of the first points made is the justification for using a soft metal such as brass:

The fracture in the shells always initiates at the inner surface below the loading contact at the convex (outer) surface. Producing a highly uniform stress distribution under the loading contact area is necessary to accurately evaluate the fracture stress from the measured fracture load data by using an analytical solution. Finite element analysis confirms that a relatively soft metal (brass foil) inserted between the specimen's convex surface and plunger tip produced a highly uniform stress distribution under the contact area. [5]

As demonstrated in previous research, the tool steel did not create a sizable and uniform distribution of stress. This report states that for the brass foil the stress variation is less than 10% the maximum value for the majority of the inner surface below the contact area [5]. It also states that the load-transferring area on the outside of the shell is sufficiently uniform, although no quantitative data is included. These statements are at the heart of the rationale for why the analytic solution is valid and the effective surface area is equal to the contact area. (It should be noted that the validity of the analytic solution will be reevaluated in the work contained herein.)

One of the main goals of the ORNL brass foil testing was to determine which parameters affect the fracture strength of the SiC shell. From the results of the populations tested it was stated that:

- Results indicate that grain size is not a dominant factor in determining fracture
- The inner surface roughness cannot explain the difference in fracture strength because the degree of roughness is not discernible
- Deviations in shell geometry (diameter and thickness) are not significant enough to produce a noticeable effect on the results
- The size effect (Weibull distribution input) is significant and must always be applied in the analysis

It should be noted that the shell geometry values used in calculations were population means, not individual test article measurements. Overall, one possibility suggested for why the difference in fracture strength could not be explained by microstructure properties is that the controlling factor is actually a complex “competition of effects from multiple parameters” [5]. Ultimately, the paper concludes that:

A detailed investigation is needed on this issue, focusing on discerning the influences of individual parameters. [5]

In a value added extension of this most recent research at ORNL, the type of detailed investigation requested is performed in the research contained herein.

2.3.5 Summary of Previous Research Results

In 2007, Snead et al. published their handbook of SiC properties, which contains a wealth of data on fracture strength [4]. Shown in Table 2.2 is an edited version of the original CVD SiC (Particle) table entries, where one entry has been removed, reference numbers have been changed to fit this document, and results from research performed after 2007 have been added.

Table 2.2: Summary of Strengths for Isolated CVD SiC Particle Material [4]

	Weibull modulus	Characteristic strength (MPa)	Test method	References
1	4.1-6.6	659-1412	O-ring (brittle ring)	[11]
2	3.0-5.6	1490-1730	O-ring (brittle ring)	[10]
3	4.8-9.4	1050-1890	O-ring (brittle ring)	[9]
4	4.0-9.0	980-2200	C-ring (brittle ring)	[9]
5	3-8	620-720	Hemisphere Bending	[15]
6	6.6-8.4	1870-3170	Hemisphere Bending	[16]
7	5.8-7.5	356-427	Diametrical Compression	[13][14]
8	4.3-6.2	222-321	Internal Pressurization	[13][14]
9	3.98-7.25	330-650	Diametrical Compression	[5][17]

This summary of Weibull modulus and characteristic strength contains results from over 15 publications. These are the results of destructive testing on different geometries and manufacturing processes of SiC. The entries labeled “CVD SiC (Particle)” concern the isolated SiC shell tests being studied in depth in this literature review.

2.3.6 Summary of Previous Research Conclusions

Since the first publications, numerous researchers have contributed to the overall understanding of fracture strength in the SiC layer of TRISO coated nuclear fuel particles. Listed here are some key observations and conclusions that have been made over the years:

1. Analytic solutions for stress, based on the theory of thin plates and shells, ignore shell asphericity (e.g. non-circularity in ring tests)
2. Results are in the same range as other geometries of SiC (e.g. bending tests performed on SiC strips) [4]
3. There is a wide distribution in mechanical property results (standard deviations up to 23% [7])
4. Fracture occurs by extension of inherent flaws on the surface under tension [15]
5. Flaws are associated with surface roughness and strength was increased when reducing surface roughness by adjusting manufacturing parameters [15]
6. Weibull statistical analysis must be applied to determine the equivalent strength of the whole shell, because only a small portion is being stressed [15]

Additionally, for diametrical compression tests:

1. Fracture initiates at the inner shell surface, in multi-axial hoop tension [13]
2. The stress on the inner shell surface under the contact area is not uniform and the max. principal stress is not located at the exact centroid (i.e. apex) [13]

3. A softer crush plate material, such as brass foil, produces a larger area of more uniform stress on the inner surface of the SiC shell [5]
4. Current testing has not yet determined the effects of each input parameter on the fracture strength of the SiC shell [5]

In summary, it is important to keep in mind these previous statements when engaging in a new-and-improved round of what is a relatively old research topic.

CHAPTER 3

METHODOLOGY

The research presented in this thesis is a combined effort, executed by numerous researchers at multiple institutions. In this chapter, activities concerning the complete test article production and testing life cycle are addressed. As expected, activities occurring at CSM are described in more detail than those being performed at other institutions.

3.1 TRISO Coated Particle Manufacturing

In the case of the test articles used in this research, there are two key aspects worth noting. First, the particles tested are not actually nuclear fuel. For safety purposes, the UO_2 core has been replaced by a non-fissile substitute of zirconium oxide (ZrO_2). The TRISO coating is applied using the same techniques as nuclear fuel production. Also, the SiC layer is never directly applied to the core, it is applied to a pyrolytic carbon (PyC) layer surrounding the core. Thus, there is no expected difference in the SiC layer, whether the TRISO coating is applied to the inert core or the nuclear fuel particle. Second, all test articles originate from the same source, Babcock & Wilcox. There are no intentional variations introduced in manufacturing. All samples are manufactured with the same processes, with the intent that they will have the same properties upon completion. (Samples are AGR-coated zirconia beads: Zirconia core, Lot # G73F-NF-93044A, Sample # NP-B8671.)

3.2 Test Article Preparation

The activities described in this section were performed at Boise State University under the supervision of John Youngsman and Darryl P. Butt.

3.2.1 Equipment List

The following equipment was used in the process of preparing SiC shell test articles:

1. Thermolyne Type 13100 stirring hot plate
2. Thermolyne 48000 furnace
3. Fisher Scientific FS20 sonicator

3.2.2 Procedure

The following information is a modified version of an unofficial document from Boise State researchers. The original document is used to give step-by-step instructions on how to reduce a TRISO coated particle to a single hemispherical SiC shell. (Note: brand name products may be replaced with suitable generic equivalents.)

1. Mount 6-7 TRISO coated particles onto a glass polishing slide using a hot plate and QuickstickTM 135 Mounting Wax.
 - Set hot plate temperature to 110°C, place slide on hot plate, and wait for uniform temperature to be reached
 - Apply mounting wax to the glass surface, ensuring enough is present to cover particles
 - Place TRISO coated particles in wax, remove slide from hot plate, and press down on each sample to ensure adherence
 - Allow slide and contents to cool
2. Grind and hand polish the particles until they are hemispheres (half depth)
 - Utilize 320, 800, and 1200 grit SiC paper
 - Figure-8 motion (process time is ~10 minutes)
3. Remove Zirconium dioxide (ZrO₂) cores manually with tweezers (after 1200 grit polish) if they have not fallen out already
4. Place the slide back on the hot plate and remove the samples

- Alternatively, acetone may be used to dissolve the mounting wax
5. Place half shells into an alumina boat and heat in air in a box furnace
 - 5°C/min ramp up from room temperature to 800°C
 - 5°C/min ramp down from 800°C to room temperature
 6. Verify that the wax and the inner and outer graphite layers have disappeared
 7. Sonicate the SiC hemisphere samples in Alconox[®] and deionized (DI) water (~10 minutes) and rinse with DI water
 8. Sonicate the samples in isopropyl alcohol (~10 minutes) and air dry
 9. Immerse the samples in a Buffered Oxide Etchant (BOE) (~10 minutes) and *triple rinse* with DI water
 - This process is used to remove any SiO₂ that may have formed while removing the graphite layers
 10. At this point any extra environmental steps are applied, such as irradiation or exposure to Carbon Monoxide (CO) as a corrosive

Note: There is also a slightly altered methodology in which the glass slide is replaced by a metal block with mounting dimples for the TRISO coated particles and a lip (or standoff) that rises to the approximate center-point of the spherical particles. This mounting block prevents over-grinding and gives greater assurance that the grinding and polishing phase will more consistently produce hemispheres that are closer to half the size of the original particle. This mounting block can easily be produced using a common sense machining approach and thus is not explained in further detail here.

3.3 Radio Microscopy Measurement and Inspection

The lab based activities described in this section were performed at CSM by Logan Ward. All geometric calculations were developed and implemented in conjunction with the author.

3.3.1 Equipment List

The following equipment was used in the process of measuring and inspecting SiC shells with a Scanning Electron Microscope (SEM):

1. FEI Quanta 600i Environmental SEM - used on and after 6/28/12
2. FEI Phenom G1 Desktop SEM - used before 6/28/12
3. ImageJ image processing software (and a suitable computer to run it)

3.3.2 Procedure

The following steps are used to create SEM images:

1. Apply carbon tape to the top of a standard materials mounting block (small black cylindrical disk)
2. Place a hemispherical SiC shell on the carbon tape, ground side facing up
3. Adjust shell so that the flat ground surface is horizontal and place in SEM
4. Take "backscatter images" with the SEM (preferred as *.tiff files)
5. Remove mounting block from the SEM
6. Adjust shell so that the flat ground edge is vertical and place in SEM
7. Take "backscatter images" with the SEM
8. Remove mounting block from the SEM and remove shells from mounting block

The following steps are done with ImageJ image processing software:

1. ImageJ automatically determines the nominal radius of the shell by calculating it from the cross sectional area of the ground surface

2. Maximum and minimum radius are also automatically calculated as the nearest and furthest circumferential point from the centroid of the cross-sectional area
3. There is a manual "node count" where the number of nodes is counted from the clearly visible maximum radii in the shell
4. Height is measured by manually constructing perpendicular lines to measure height from the base
5. Shell thickness is manually measured at 8 points which are approximately evenly spaced, but ultimately chosen for clarity of the edges in the image
6. Notes are included in the measurement data if there are chipped edges and/or cracks in the shell

3.3.3 Geometric Calculations

At the conclusion of the measurement and inspection procedure in the lab, there are sets of data that cannot be directly used (e.g. each shell has 8 values for thickness). Thus, additional mathematical work must be performed so that this data can be converted into usable information. In the case of geometric data, each test article must have an individual nominal value and error for the ideal hemispherical shell characteristics of: height, outer radius, and thickness.

The height of the sphere is only measured once and there is not a well defined error that can be attributed to it. This height will only be used in adjusting values of outer radius and thickness because those measurements might not be made on a cross-section passing through the center point of an ideal sphere [18]. Any reasonable error in the height, such as 1% or 5%, results in a very negligible error propagation to the adjusted values. Thus, the height measurement is considered to have no error.

The outer radius measurements from the lab procedure are expressed as R_{Mmin} , R_{Max} , and R_{Mmax} . These measurements are taken from the cut and polished cross section of the

test article. Shown in Figure 3.1 is an exaggerated example of how an off center cross section does not give accurate values for spherical dimensions.

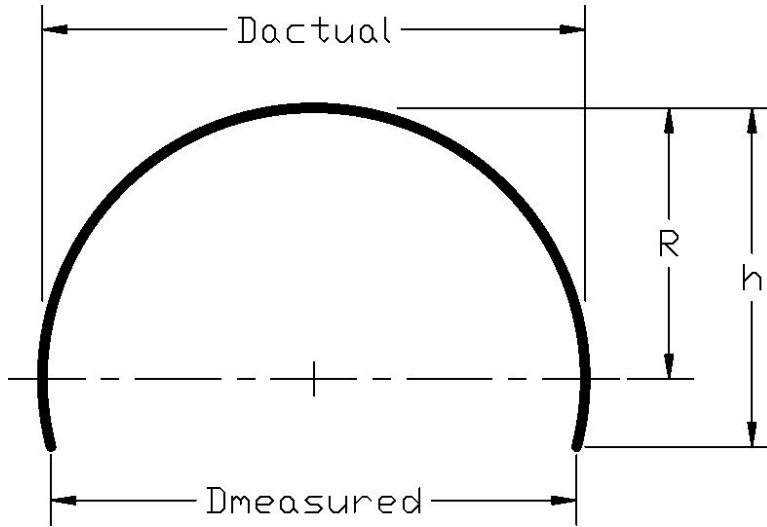


Figure 3.1: Difference Between Measured and Actual Diameter

Equation (3.1) represents the mathematical adjustment of outer radius shown in Figure 3.1. It is based on equations relating the chord and sagitta of a circle [19].

$$R = \frac{\left[R_{Mav} - |R_{Mav} - h| \right]^2 + R_{Mav}^2}{2(R_{Mav} - |R_{Mav} - h|)} \quad (3.1)$$

Where:

h = hemisphere height

R_{Mav} = average measured shell outside radius

R = nominal shell outside radius

Additionally, the difference between R_{Mmin} and R_{Mmax} can be defined as some number of standard deviations. By engineering judgment, defining this difference as 4 standard deviations (encompassing $\sim 95\%$ of the population) is a little overconfident. Instead it will be defined as 2 standard deviations and one standard deviation will be used as the error for

outer radius in future equations. This is shown numerically in Equation (3.2). (Note: In later equations, μ and σ are used as an intermediate variable and stress, respectively. Thus, these symbols are not used in any of the statistical or error propagation equations.)

$$\delta R = \frac{R_{Mmax} - R_{Mmin}}{2} \quad (3.2)$$

Where:

R_{Mmin} = minimum measured shell outside radius

R_{Mmax} = maximum measured shell outside radius

Shell thickness requires more steps to calculate a nominal value and error. Initially, 8 values are used in the standard statistical equations for arithmetic mean and sample standard deviation, shown in Equations (3.3) & (3.4).

$$\bar{x} = \frac{1}{n} \cdot \sum_{i=1}^n x_i \quad (3.3)$$

$$s = \sqrt{\frac{1}{n-1} \cdot \sum_{i=1}^n (x_i - \bar{x})^2} \quad (3.4)$$

Where:

n = number of samples

i = sample index

x_i = indexed sample value

The 8 measured values are taken from a single plane in the hemisphere, meaning that they do not necessarily represent an envelope of 95% or 99% of the thickness values throughout the shell. Therefore, one standard deviation is taken to be the measurement error. Relabeling the results of Equations (3.3) & (3.4), the measured thickness value is shown symbolically in Equation (3.5).

$$t_M^- \pm \delta t_M^- = \bar{x} \pm s \quad (3.5)$$

Where:

t_M^- = mean measured shell thickness

Similar to the outer radius, thickness values must also be adjusted for off-centerline measurements. For simplicity, the equation to adjust these values (Equation (3.6)) is the same for both t_M^- and δt_M^- when the appropriate value is substituted in.

$$t = t_M^- \sqrt{1 + \left(\frac{|R_{Mav} - h|}{R} \right)^2} \quad (3.6)$$

Where:

t = nominal shell thickness

Thus, for use in future calculations and error propagation, both $R \pm \delta R$ and $t \pm \delta t$ for each test article have been defined.

3.3.4 Limitations and Systematic Errors

In measuring test articles, it is evident that there are limitations created by quantifying the shell geometry with two parameters, R and t . While not all-inclusive, some sources of limitations and systematic errors are:

- Resolution limitations caused by the pixel size of electronic images
- Increased variance from human error in performing measurements
- Skewed data from articles not being perfectly parallel to the imaging device
- Base section measurement deviation from dimensions at the apex of the shell
- Local measurement deviation from an unquantifiable average measurement

Regardless of any additional limitations and systematic errors, there is one that is qualitatively more significant than any other: shell asphericity. This is exemplified by the SEM image in Figure 3.2.

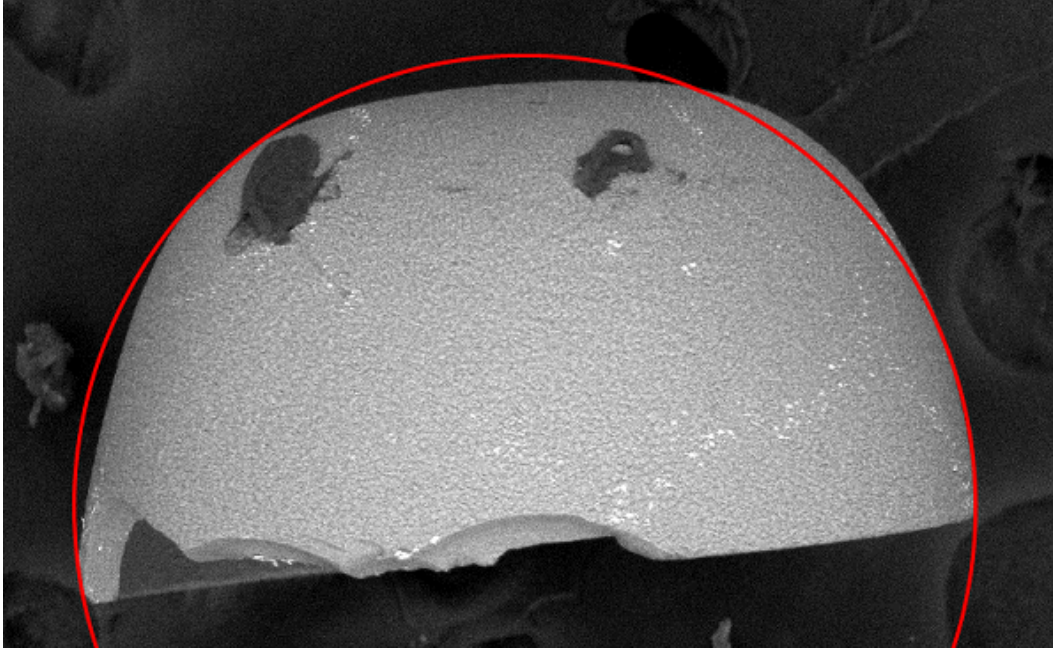


Figure 3.2: Qualitative Example SEM Image of Test Article Asphericity

For this test article, the local outer radius at the apex of the shell is clearly much larger than any estimated average. This larger radius is located at the small portion of the shell which is stressed during fracture testing. Hence, this shell will displace less indenter material and create a larger divot radius than a perfectly spherical shell. Thus, any other limitations or systematic errors are qualitatively minor in comparison to the inherent asphericity of the shell.

3.4 Load Cell Crush Tests

The lab based activities described in this section were performed at CSM by Logan Ward.

3.4.1 Equipment List

1. Ernest F. Fullam, FEI Tensile Testing Substage with Data Acquisition Control System (No. 18239)
2. Sensotec, 10 lb. Capacity Load Cell (PN 060-1127-05; Model 11; SN 1072953)
3. Measurements Group, Linear Displacement Sensor (Model HS24; SN MG5229)

- The displacement sensor was attached, but the data collected was not used

3.4.2 Procedure

The following steps are performed during crush testing. Also included in the steps are specific notes about equipment modifications and data collection.

1. Place SiC shell test article in acetone bath, remove, and air dry
2. Attach pieces of double sided tape all around the outer edges of the bottom ram
 - This tape is used to catch broken pieces of the crushed shell
 - Care must be taken to ensure tape is not in the load cell ram path in a way that will skew data
3. Verify that the top ram has the appropriate type of polished annealed metal attached to it's surface with CrystalbondTM
 - In tests performed in this research, copper, brass, or nickel were used
 - The metal on the top ram has labels along the side, creating “zones” so that a crush test can later be matched to its individual divot
4. Bolt rams in place in the crush test fixture
5. Move the fixture crosshead in “adjustment mode” until the ram is close, but not touching, the test article
6. Start crush test routine with fixture control software
 - The test is force controlled (not displacement controlled) at 3 N/min
7. Manually stop the crush test after completion
 - The test is complete when one can hear the “pop” of the test article breaking and can see the load cell force go down on the realtime monitor output

8. Remove bottom ram, then collect and store test article pieces in an individually labeled container

- The SEM will be used later to determine divot size on the crush plate

It should be noted that there are various calibration procedures performed to ensure that the crush test load cell measurement system produces accurate and precise data (even though all applicable equipment also has 3rd party calibration certificates). These procedures should be tailored to any specific equipment used to replicate this test and it may not be best to blindly mimic the same calibration for slightly different equipment.

In the case of these tests, the load cell is located under the bottom ram. A calibration is performed with 3 weights (~1 lb., ~2 lb., ~6 lb.) which are measured on a calibrated scale and then placed on the bottom ram of the test fixture. This calibration is performed before each round of tests. The data acquisition system also has the ability to bypass the load cell and apply a dummy electronic load in order to calibrate itself. This calibration is rarely performed as it is redundant and only tests part of the system. In no cases have there been calibrations of any kind that grossly contradicted previous calibrations or settings.

3.5 Post-Test Measurement and Inspection

The lab based activities described in this section were performed at CSM by Logan Ward. All geometric calculations were developed and implemented in conjunction with the author.

3.5.1 Equipment List

1. FEI Quanta 600i Environmental SEM - used on and after 6/28/12
2. FEI Phenom G1 Desktop SEM - used before 6/28/12
3. ImageJ image processing software (and a suitable computer to run it)

3.5.2 Procedure

The following steps are used to create SEM images:

1. Place whole crush plate into SEM
2. Using recorded data on crush plate zones, locate the specific test article divot
3. Take “backscatter images” with the SEM (preferred as *.tiff files)

The following steps are done with ImageJ image processing software:

1. Manually trace the edge of the divot
2. Refine traced line with Fourier smoothing plug-in
3. Convert image to binary format with a black divot area and white background
4. Determine average radius (r_{av}) from the black area in the binary image
5. Measure extremes from the centroid using the “Draw minR & maxR” plug-in to calculate the values r_{min} & r_{max})

3.6 Numerical Analysis

The primary goal of this research is to determine the fracture strength of the SiC shell in a TRISO coating. As a ceramic, the SiC experiences brittle fracture and the fracture strength is the maximum principal stress that results in a crack propagating through the material. Due to the size of the test article, stress in the material at the point of fracture will not be directly measured (e.g. strain gauge). Thus, numerical analysis must be used to determine fracture strength.

Each numerical analysis technique must be considered an open loop solution, as there is no direct measurement which can verify the results. Thus, in order to improve assurance in the results, multiple numerical methods will be employed. An exact analytic solution to a plate and shell theory PDE will be solved. Several methods of error propagation will be used to produce results in the form of an expected value with error (e.g. mean and standard deviation). A flow chart of the analytic solution methods is shown in Figure 3.3.

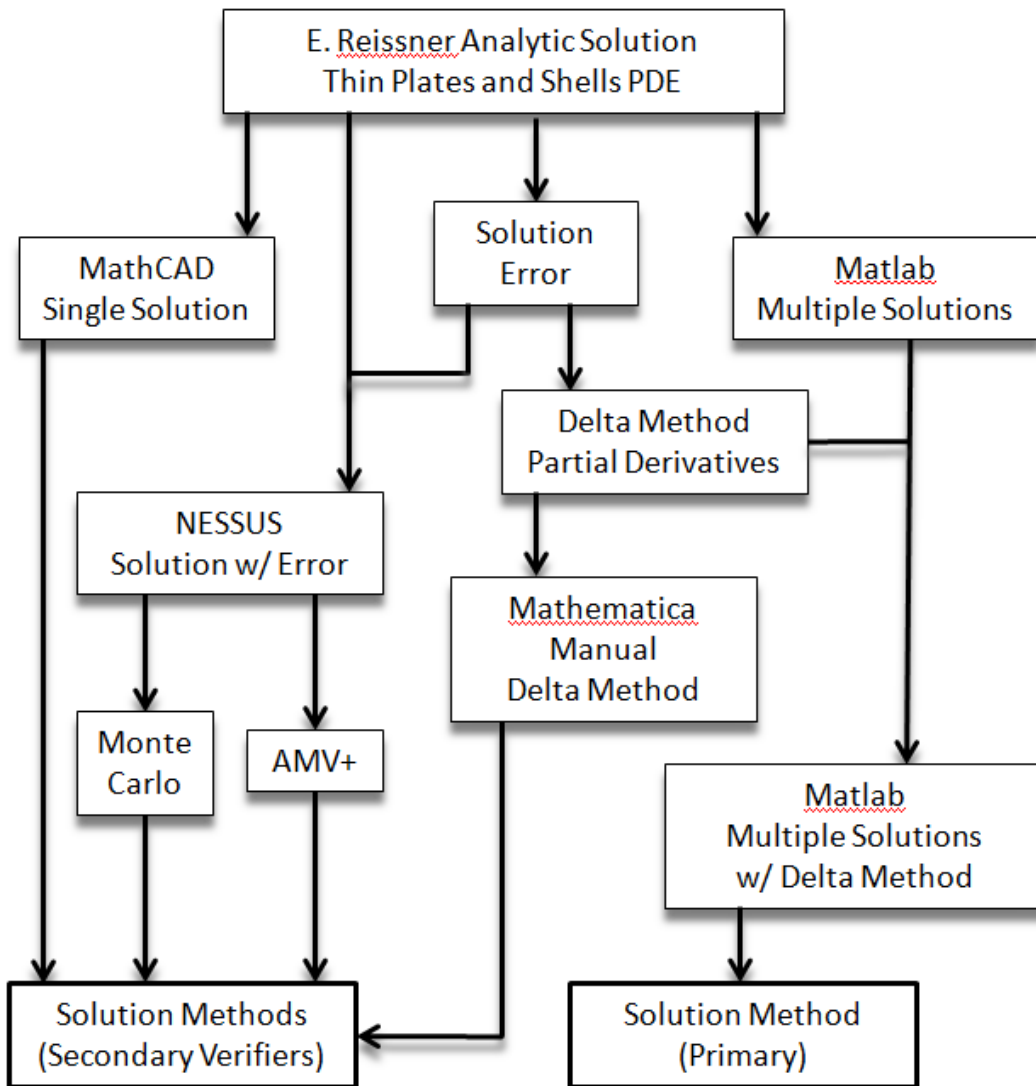


Figure 3.3: Process Flow Diagram for Analytic Solution Methods

A 3D FEA solution using the commercial software package Abaqus will also be performed. Error can be propagated through the FEA solution using NESSUS statistical software. Additional NESSUS results will be used to perform an input variable sensitivity analysis. To complete the overall numerical analysis process, differences in the results will be reconciled through discussion and conclusions will be made. A flow chart showing the overall process is shown in Figure 3.4.

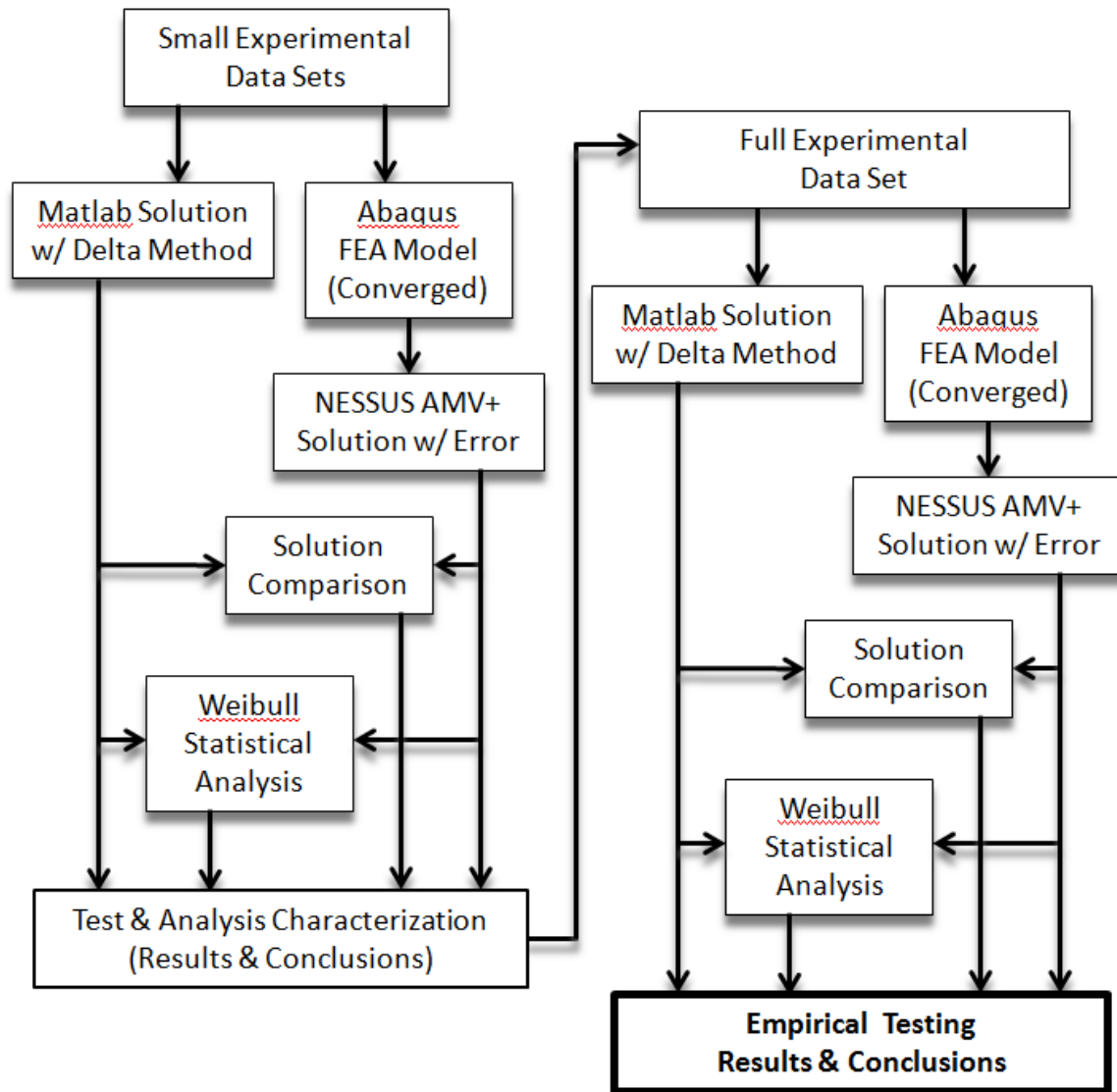


Figure 3.4: Process Flow Diagram for all Experimental Data Solution Methods

As it is a necessary early step in the overall process, the numerical analysis methods will also be utilized to better understand the diametrical compression test. This includes plotting linearly interpolated curves to determine the behavior of stress in the material beyond what individual experimental data points can convey. These results will be used to improve test design and verify analysis so they provide more accurate and precise results in this research and the future.

3.6.1 Analytic Solution

In order to create an exact analytic solution to the crush test being performed, a simplified scenario must be proposed. This diagram is shown in Figure 3.5.

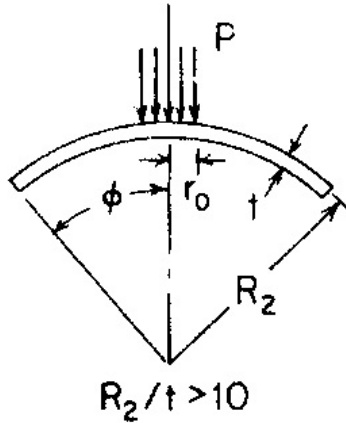


Figure 3.5: Diagram for Analytic Solution Scenario [20]

It should be noted that several conditions must be met:

- Shell thickness must be less than 10% outside radius, making theory of plates and shells produce a reasonable approximation for uniform stress.
- Angular depth of the shell (ϕ) must meet the constraint in Equation (3.13). If this is met, the shell can have any type of edge support.

Also, several simplifications are used to facilitate a solution:

- The shell is assumed to be perfectly spherical and have uniform thickness.
- Force is assumed to be an evenly distributed pressure on the outer shell surface.

While this is not a perfect representation of the crush test, this is the closest practical estimate which facilitates an exact analytic solution.

If Figure 3.5 is expressed mathematically using theory of plates and shells, there is a readily available exact solution to the Laplacian PDE [21]. Much of the final solution has

been reprinted in more recent versions of professional reference books [20]. Due to the complexity of the solution, it is traditionally expressed using six equations, where the results of former equations are substituted into latter ones. This is shown in Equations (3.7) - (3.12). It is important to note that Equation (3.12) is not part of the original E. Reissner solution; it can be found in a more recent publication from ORNL [17].

$$\mu = r_0 \left[\frac{12(1-\nu^2)}{R_2^2 t^2} \right]^{\frac{1}{4}} \quad (3.7)$$

$$C_1 = 0.2205 - 0.04\mu - 0.0115\mu^2 \quad (3.8)$$

$$C_2 = 1.2044e^{-1.2703\mu} \quad (3.9)$$

$$\sigma_{membrane} = \frac{-C_1 P \sqrt{1-\nu^2}}{t^2} \quad (3.10)$$

$$\sigma_{bending} = \frac{-C_2 P (1+\nu)}{t^2} \quad (3.11)$$

$$\sigma_t = \sigma_{membrane} - \sigma_{bending} \quad (3.12)$$

$$\phi > \arcsin \left(1.65 \sqrt{\frac{t}{R_2}} \right) \quad (3.13)$$

Where:

r_0 = Radius of Distributed Pressure

R_2 = Spherical Shell Outside Radius

t = Spherical Shell Thickness

P = Resultant Applied Force from Distributed Pressure

ν = Poisson's Ratio of Spherical Shell Material

ϕ = Angular Depth of Spherical Shell (Typical result: $90^\circ > 30^\circ$)

It can be seen that this solution produces one value for stress. This value is the maximum principal stress on the inner surface of the shell, located at the centroid of the pressure distribution (i.e. the apex of the hemisphere). This maximum principal stress represents an

equibiaxial stress state where stress is equal in all directions on a tangential 2D plane. As previously stated, this stress is not necessarily the largest maximum principal stress for the entire SiC shell.

For error propagation using the delta method, resulting error is conservatively high unless the solution is expressed as one equation. This equation for max. principal stress at the inner-apex of the shell is shown in Equation (3.14).

$$\sigma_t = - \left(0.2205 - 0.04r_0 \left[\frac{12(1-\nu^2)}{R_2^2 t^2} \right]^{\frac{1}{4}} - 0.0115r_0^2 \left[\frac{12(1-\nu^2)}{R_2^2 t^2} \right]^{\frac{1}{2}} \right) \frac{P\sqrt{1-\nu^2}}{t^2} + \left(1.2044e^{-1.2703 \left[\frac{12(1-\nu^2)}{R_2^2 t^2} \right]^{\frac{1}{4}}} \right) \frac{P(1+\nu)}{t^2} \quad (3.14)$$

Because Equation (3.14) is not linear, it is not ideal for the delta method [22], which is actually a simplified version of a Taylor expansion. Regardless, when the expected value (mean) of each input variable is used, the output is the expected value. This result for expected value is technically an “estimator” of that value. While it is often labeled the deterministic solution in engineering practice, this value is actually a biased estimator [22]. However, it will be shown in the results section that Equation (3.14) has a relatively small bias and produces results for expected value similar to other methods, such as a more accurate Monte Carlo simulation.

3.6.1.1 Linearly Interpolated Curve

The analytic solution has previously been proposed for use on experimental data points. In order to better understand the diametric compression test, one must generate a large set of linearly interpolated discrete values which appear to be a continuous curve to the casual observer. While the few experimental data points can be connected with standard curve fitting equations, that curve doesn't necessarily extrapolate accurately to show the overall nature of the analytic solution. Thus, Equations (3.7) - (3.12) can be solved with a small ΔP to create a plot for σ_t vs. P .

For this linearly interpolated curve, both R_2 and t can be defined as the mean value of the test sample population. Poisson's ratio is considered to be constant. As P is the x-axis, there is only one more variable to define, r_0 . The relation of r_0 vs. P is linked to the material properties of the crush plate and because the Brinell scale is out of range for the forces and hemisphere sizes given, there is no existing equation to use. Additionally, it is evident that polynomial curve fits do not match 3D FEA theoretical data. Instead, as it is demonstrated in the results of the 3D FEA linearly interpolated curve, the appropriate curve fitting equation for r_0 vs. P is the power law relationship shown in Equation (3.15). This equation has two constants which are dependent on material properties. Because the curve fitting system is overdetermined, the values for these constants are calculated by minimizing the residual.

$$r_0 = KP^n \tag{3.15}$$

Where:

K = Coefficient Constant

n = Power Constant

This power law relation is used to define r_0 in terms of P , thus completing the definition for all input variables required by Equations (3.7) - (3.12). On a side note, Equation (3.15) has the same form as the Hollomon equation, which approximates true stress vs. true strain [23].

3.6.1.2 Error Analysis

The general concept for standard engineering error propagation (i.e. delta method) is that the input values all have an expected value and standard deviation. Thus, the final result also has an expected value and standard deviation. In a normal distribution, one standard deviation defines the location in the Cumulative Distribution Function (CDF) at 15.9% and 84.1% probability ($\sigma_t \pm \delta\sigma_t = 50\% \pm 34.1\%$). Unfortunately, because Equation

(3.14) is not linear and error propagating equations are only being approximated by a few terms in a Taylor expansion, the resulting CDF of σ_t is not an exact solution and therefore $\sigma_t \pm \delta\sigma_t$ is an estimator. To investigate this further, several methods of error propagation will be attempted.

First, NESSUS will be used to perform a Monte Carlo analysis. Due to the simplicity of Equations (3.7) - (3.12), all calculations can be performed internally, reducing wall time in comparison to using an outside program call and temporary data file. Monte Carlo analyses will be performed at intervals between 10 – 5,000,000 points. The resulting data can be queried to determine the values of σ_t which result in 15.9%, 50%, and 84.1% probability in the CDF (i.e. mean and standard deviation). A Monte Carlo simulation never solves the equation deterministically. Thus, the difference between the 50% probability value and the deterministic solution can give an idea of how biased other methods are in estimating the expected value of σ_t .

Second, NESSUS will be used to perform the Advanced Mean Value Plus Iterations method (AMV+). An explanation of this method is beyond the scope of this section; however, it can be found in existing literature [24]. It is important to note that the 50% probability value is generated from the deterministic solution and thus it has the same bias as the delta method. However, 15.9% and 84.1% results will be compared to Monte Carlo results in order to assess their unique accuracy.

Third, even though Equation (3.14) is not linear, the delta method will be used to propagate error through this equation. It is important to note that this method produces results in a normal distribution with no skewness. The result at 50% probability is the deterministic solution, which is a biased estimator. The values at 15.9% and 84.1% probability are determined by a single standard deviation value. These results will be compared to the Monte Carlo simulation and AMV+ solution. Due to the simplicity of implementation in MATLAB scripts, this method will be employed if it is deemed sufficiently accurate. The delta method is shown in Equations (3.16) - (3.22), where some coefficients produced by

Mathematica symbolic partial derivative solutions have been rounded to 5 decimal places. In the following equations, standard deviation (error) is expressed by the symbol δ because the usual symbol (σ) also represents stress.

$$\delta\sigma_t = \sqrt{\left(\frac{\partial\sigma_t}{\partial r_0}\right)^2 (\delta r_0)^2 + \left(\frac{\partial\sigma_t}{\partial P}\right)^2 (\delta P)^2 + \left(\frac{\partial\sigma_t}{\partial \nu}\right)^2 (\delta \nu)^2 + \left(\frac{\partial\sigma_t}{\partial R_2}\right)^2 (\delta R_2)^2 + \left(\frac{\partial\sigma_t}{\partial t}\right)^2 (\delta t)^2} \quad (3.16)$$

$$\eta = \left(\frac{1 - \nu^2}{R_2^2 t^2}\right)^{\frac{1}{4}} \quad (3.17)$$

$$\begin{aligned} \frac{\partial\sigma_t}{\partial r_0} = & -\frac{2.84756 \cdot P\eta(1 + \nu) \cdot e^{-2.36429r_0\eta}}{t^2} \\ & + \frac{P\sqrt{1 - \nu^2}(0.07445\eta + 0.07967r_0\eta^2)}{t^2} \end{aligned} \quad (3.18)$$

$$\begin{aligned} \frac{\partial\sigma_t}{\partial P} = & \frac{\sqrt{1 - \nu^2}(-0.02205 + 0.07445r_0\eta + 0.03984(r_0\eta)^2)}{t^2} \\ & + \frac{1.2044 \cdot (1 + \nu) \cdot e^{-2.36429r_0\eta}}{t^2} \end{aligned} \quad (3.19)$$

$$\begin{aligned} \frac{\partial\sigma_t}{\partial \nu} = & -\frac{P\nu(-0.02205 + 0.07445r_0\eta + 0.03984(r_0\eta)^2)}{t^2\sqrt{1 - \nu^2}} \\ & + \frac{1.42378 \cdot Pr_0\nu(1 + \nu) \cdot e^{-2.36429r_0\eta}}{R_2^2 t^4 \eta^3} \\ & + \frac{P\sqrt{1 - \nu^2}\left(-\frac{0.03722r_0\nu}{R_2^2 t^2 \eta^3} - \frac{0.03984r_0^2\nu}{R_2^2 t^2 \eta^2}\right)}{t^2} \\ & + \frac{1.2044 \cdot P \cdot e^{-2.36429r_0\eta}}{t^2} \end{aligned} \quad (3.20)$$

$$\begin{aligned} \frac{\partial\sigma_t}{\partial R_2} = & \frac{1.42378 \cdot Pr_0(1 + \nu)(1 - \nu^2) \cdot e^{-2.36429r_0\eta}}{R_2^2 t^4 \eta^3} \\ & + \frac{P\sqrt{1 - \nu^2}\left(-\frac{0.03722r_0(1 - \nu^2)}{R_2^3 t^2 \eta^3} - \frac{0.03984r_0^2(1 - \nu^2)}{R_2^3 t^2 \eta^2}\right)}{t^2} \end{aligned} \quad (3.21)$$

$$\begin{aligned}
\frac{\partial \sigma_t}{\partial t} = & -\frac{2P\sqrt{1-\nu^2}(-0.02205 + 0.07445r_0\eta + 0.03984(r_0\eta)^2)}{t^3} \\
& -\frac{1.42378 \cdot Pr_0(1+\nu)(1-\nu^2) \cdot e^{-2.36429r_0\eta}}{t^2} \\
& +\frac{P\sqrt{1-\nu^2}\left(-\frac{0.03722r_0(1-\nu^2)}{R_2^2t^3\eta^3} - \frac{0.03984r_0^2(1-\nu^2)}{R_2^2t^3\eta^2}\right)}{t^2} \\
& -\frac{2.4088 \cdot P(1+\nu) \cdot e^{-2.36429r_0\eta}}{t^3}
\end{aligned} \tag{3.22}$$

In conclusion, it will never be possible to know the exact values of σ_t at 15.9%, 50%, and 84.1% probability in the CDF. This should not be unsettling for several reasons: some errors, such as Poisson's ratio, are only rough estimates; the pressure distribution acting on the shell is a simplified uniform value which does not exactly represent reality; and the perfect spherical shell in the analytic solution is not an exact representation of the aspherical shells being tested. The assumptions the analytic solution makes far outweigh the small inaccuracies in the propagation of error. Still, significant due diligence is performed because it does not add to project cost, it reduces stacking of mathematically induced errors, and it is feasible. Ultimately, the Monte Carlo simulation with 5×10^6 points will be assumed to give the most accurate results and any other results will be compared to those values.

3.6.1.3 Sensitivity Analysis

One of the benefits of using NESSUS is the built-in solvers for input variable sensitivity analysis [25]. This information is readily displayed in the results of any Monte Carlo simulation or AMV+ solution. Due to the non-linear nature of Equation (3.14), these sensitivity values change for different σ_t magnitudes. In some cases a single graph will show results across a range of σ_t values. In the cases where results are available at different σ_t values, they will primarily be evaluated at the mean. All NESSUS sensitivity results will be interpreted as relative values, only meant to understand which input variables are more significant than others. In addition to using NESSUS, a table comparing terms in Equation

(3.16) will be constructed as a manual verifier of which input variables contribute the most to output error. This table will contain the results of functions that are evaluated at input variable means.

3.6.1.4 Divot Asphericity

As previously stated, the analytic solution requires an assumption to neglect shell asphericity. Since the shell is not spherical, the divot in the crush plate is not spherical and the distributed load cannot be accurately characterized by a single r_0 value. Rather, it is characterized by r_{min} , r_{av} , and r_{max} values. Due to analytic solution constraints, these multiple parameters cannot be used. Instead, the results of the analytic solution can be plotted against the dimensionless asphericity value defined in Equation (3.23).

$$r_{asp} = \frac{r_{max} - r_{min}}{r_{av}} \quad (3.23)$$

Where:

r_{av} = Average Measured Radius

r_{min} = Minimum Measured Radius

r_{max} = Maximum Measured Radius

This dimensionless asphericity value is used to qualitatively assess how far the loading condition deviates from the analytic solution. The results section shows cases where this value can be used to remove data points that would not be recognized as outliers by only evaluating σ_t values.

3.6.2 3D Finite Element Analysis

This stress study cannot be considered complete without an application of the finite element method (FEM). Researchers at ORNL have previously solved two different FEA models and published their results [13] [17]. In each case there are simplifications for reducing calculation times (e.g. 2D geometry, symmetric boundary conditions). Due to the

exceptional computer resources available at CSM, these simplifications are not necessary. A full 3D model of the shell and crush plate can be simulated while reasonable accuracy and computation times are maintained. (Note: In the FEA, the crush plate is also referred to as the indenter.) The commercial software package Abaqus will be used as the FEA solver and screenshots of the general model are shown in Figure 3.6.

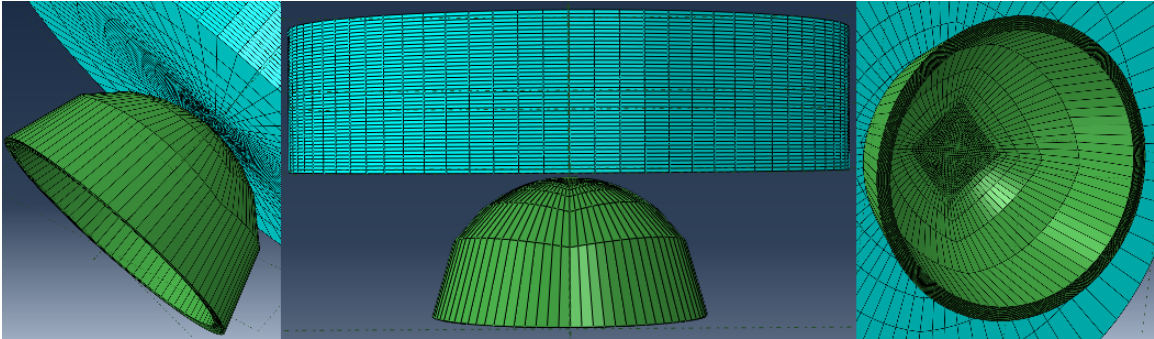


Figure 3.6: Screenshot of FEA Model and Element Discretization

This model and discretization selection is rationalized by several key points:

1. Entire test is modeled (no geometry or boundary condition simplifications)
2. Contact area is refined (better accuracy with fewer elements)
3. Indenter is larger than the shell (reduced boundary condition effects)

There are also some technical details of the model which are worth noting:

1. The Abaqus “standard” solver is used. This solver generates a stiffness matrix and calculates displacements. Contact deformation is calculated by removing overclosures between contact elements.
2. When no element type is specified, Abaqus applies a default. In the discretization used, this is a linear 8-node hexahedron element with reduced integration (C3D8R).
3. For quadratic elements, Abaqus chooses between 3 element types (C3D20R, C3D15, C3D10) based on element shape. These are 20-node hexahedron, 15-node triangular

prism, and 10-node tetrahedral, respectively. In the discretization used, elements are of the 20-node hexahedron reduced integration variety.

4. The indenter Boundary Condition (BC) fixes 5 Degrees of Freedom (DOF) on the flat face furthest from the shell. The 6th DOF is the position value used to control indent depth.
5. The shell BC fixes the surface at the bottom of the shell in all 3 positional DOFs (rotational DOFs are not constrained). This is consistent with the test condition of a shell resting on a flat surface.
6. There is no specific friction algorithm used, resulting in the default of frictionless contact. While the actual test conditions support friction on the contact surface, plastic deformation of the brass renders friction effects negligible due to the unhindered flow of material directly beneath the friction surface.
7. This model assumes there is no residual stress in the SiC shell. Without specific information concerning the introduction of residual stresses in manufacturing and processing of test articles, this is a necessary assumption.
8. It should be noted that this is not a fracture mechanics model.

Beyond these points, one of the most important aspects of using an FEA model is properly defining the materials involved.

3.6.2.1 Material Properties

Reference values of ν and E for the SiC shell are used in other analysis methods. They are located in the literature review section and Abaqus requires no more information on the SiC because the shell experiences brittle fracture. Specifically for Abaqus, the indenter material is defined in a CSV file using a reference value for ν along with experimentally determined values for E and a true stress vs. true plastic strain curve. Initially, raw data

is generated from an experimental true stress vs. true strain test performed on the indenter material. This data is then split into parts using MATLAB (i.e. elastic, early plastic, late plastic, extrapolation) and different methods are used to format each section for Abaqus. A visualization of the four sections, with empirical plastic strain data highlighted, is shown in Figure 3.7.

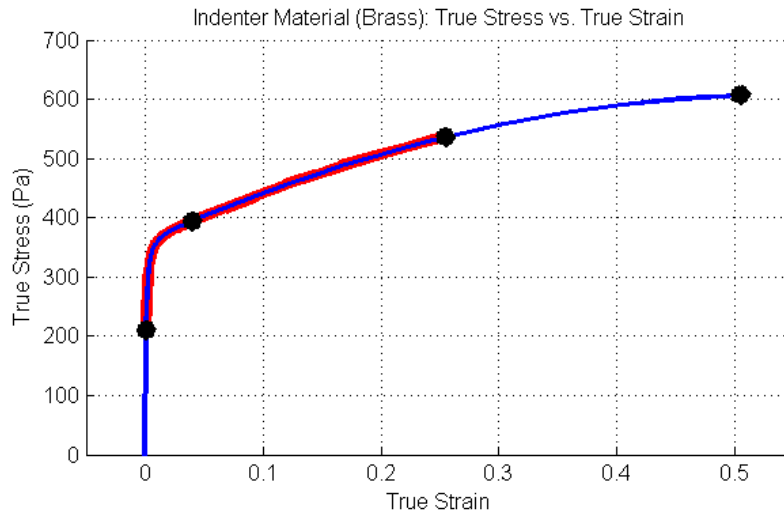


Figure 3.7: Sample Indenter Material Curve with 4 Distinct Sections

The MATLAB script itself contains the exact numerical methodology used in reformatting the experimental curve. However, a basic explanation is given here:

1. E is determined by semi-manually gaging where the slope of the curve starts to change and then taking a mean of the slopes before that point. ($E = 178GPa$)
2. The beginning of the early plastic section ($\sigma_{p1}, \epsilon_{p1}$) is determined by slightly offsetting E on the positive x-axis and finding its intersection with the curve.
3. The data in the early plastic section is smoothed by sampling every other point. The end of this section is manually chosen.
4. The data in the late plastic section is smoothed by sampling every 150th point. This helps maintain the Abaqus requirement of an ever-increasing curve.

5. The final point from the experimental data is added to the new curve, thus completing the late plastic section.
6. Each data point $(\sigma_{pi}, \epsilon_{pi})$ is shifted by the strain where plasticity begins (ϵ_{p1}) to create the Abaqus curve of true stress vs. true plastic strain $(\sigma_{pi}, \epsilon_{pi} - \epsilon_{p1})$.
7. A polynomial curve fit is made of the shifted late plastic section and it is used to extend the curve from the last point to a higher plastic strain ($\epsilon_{pf} = 0.54$)

At the end of this process, the MATLAB curve is manually cut-and-paste into a CSV file that already contains E and ν for both the indenter material and SiC shell. This file is directly read by Abaqus each time an analysis is run. Still, before the general FEA model can be used to generate test results on actual experimental data points, the multiple parameters for element discretization must be systematically refined through convergence studies.

3.6.2.2 Convergence Studies

In commercial applications, convergence studies often involve a simple one-parameter study where a generic variable labeled “refinement” is increased and results are compared. In the case of this academic work, there are 11 parameters that define element discretization. Each parameter has varying individual effects, as well as effects that are seen when combined with other parameters. The multiple inputs to this parametric convergence study are:

- Shell Element Discretization (i.e. Circumferential Elements, Thickness Elements, Radial Elements, Radial Element Bias)
- Indenter Element Discretization (i.e. Circumferential Elements, Thickness Elements, Radial Elements, Radial Element Bias)
- Indenter Size (i.e. Thickness, Radius)
- Refinement Zone Size (One Parameter, Same for Shell & Indenter)

There are several features of the element configuration that can be immediately noted:

1. Contact area element discretization is defined by the number of circumferential elements and refinement zone size (independent of the shell or indenter radius).
2. Element length in thickness and the aforementioned contact area discretization determines element aspect ratios in the refinement zone.
3. Radial element discretization should not significantly affect the results in the contact area, so long as the refinement zone is a sufficient size.

In addition to part size and element discretization, Abaqus has several analysis options that are included in the parametric study:

1. `nlgeom` (yes or no): allows non-linear geometry in the model
2. `unsymmetric` (yes or no): allows the solver to use an unsymmetrical matrix
3. `element` (linear or quadratic): defines the polynomial equations used to define nodes and solve nodal displacements in each element
4. `contact` (general or surface-to-surface): defines the way in which overclosure is calculated before each part is deformed to remove it

With so many options in the parametric study, it is reassuring to know some aspects of the 3D FEA solution do not change. First, the solver used will be Abaqus standard. This solver generates a stiffness matrix and then solves for nodal displacements. Stress and other parameters are calculated after displacements. Second, the only element shape used will be hexahedral. Wedge elements used in prototype testing (not reported herein) were removed due to their questionable behavior in contact problems.

Due to the number of parameters involved, there will be several different convergence studies. There are numerous small preliminary convergence studies (not reported in this

document) which will be used to gain a general feel of how the model functions in Abaqus and to weed out poor solution tactics (e.g. defining dimensions in meters). The intermediate convergence studies will be performed to determine the general behavior of the model and its response to changes in element discretization. The main convergence study will contain the rationale for the final element discretization(s) used. It features variations in key parameters and also contains subsets within the study which vary the Abaqus options and evaluate their influence, if any. Finally, the result of the entire convergence study process will be configuration controlled Abaqus python script(s) which define both element discretization and analysis options. These script(s) will be used to create 3D FEA models which will be compared to results from other techniques and researchers.

3.6.2.3 Accurate Divot Size

Experimentally measured divot size is an input value of the analytic solution. Unfortunately, it is not possible to directly prescribe a divot size so that Abaqus moves the indenter until it is reached. Instead, Abaqus requires an input for linear displacement of the indenter. Essentially, this value is the initial gap between the indenter and shell, plus divot depth. Thus, a prescribed divot depth must be defined in terms of the desired divot radius. If we maintain our previous assumption of a spherical shell and also assume elastic flexing of the shell and elastic rebound of the indenter are both negligible, then the appropriate equation is the sagitta in terms of a chord [19]. This is shown in Equation (3.24) where l_d is the sagitta, r_{av} is half of the chord, and R_2 is the circle radius.

$$l_d = R_2 - \sqrt{(R_2)^2 - (r_{av})^2} \quad (3.24)$$

Where:

l_d = Theoretical Divot Depth

r_{av} = Average Measured Divot Radius

R_2 = Shell Outside Radius

In preliminary FEA testing (not reported herein), it was found that elastic flexing of the shell has a significant impact on the relationship between prescribed divot depth and resulting divot radius. The elastic rebound of the indenter material is not significant, but does contribute. Accurately quantifying these effects through theoretical means is far beyond the scope of this research. Instead, the curve for prescribed divot depth vs. divot radius will be estimated by Equation (3.24) offset by a constant. This is shown in Equation (3.25), where C_{adj} is expected to vary with test parameters and will be determined by a minimum residual curve fit to FEA results.

$$l_{da} = R_2 - \sqrt{(R_2)^2 - (r_{av})^2} + C_{adj} \quad (3.25)$$

Where:

l_{da} = FEA Prescribed Divot Depth

C_{adj} = Curve Shifting Constant

Equation (3.25) will be included in Abaqus scripting, where the user inputs values for r_{av} and C_{adj} and the script automatically calculates a proper indenter displacement value. This will ensure that the FEA divot radius (r_d) in the final frame is close to the experimentally determined value (r_{av}). Having these two values match is crucial to effectively utilizing NESSUS, which only queries results from the final frame.

3.6.2.4 Linearly Interpolated Curve

Similar to the analytic solution, Abaqus FEA can be used to create a linearly interpolated curve. Due to longer calculation times and semi-manual data extraction, the FEA version will have significantly fewer data points than its analytic counterpart. However, the overall premise is the same. In the case of the Abaqus python script, l_d (and the subsequent r_d it creates) is an input and both F_R and σ_{pS} are outputs. These variables are the 3D FEA values for prescribed divot depth, divot radius, reaction force, and supremum principal stress, respectively. For consistency between methods, the values for t and R_2 can be taken as the

population mean. To compare the two solutions, a plot of the 3D FEA r_d vs. F_R can be compared to the results of r_0 vs. P for the analytic solution. Also, the plot of σ_{pS} vs. F_R and σ_t vs. P can be compared.

Obviously, the 3D FEA solution does not have as many limitations as the analytic solution. Specifically, it allows for a variation in pressure distribution on the surface of the shell. This pressure distribution is expected to vary because of work hardening of the indenter material. The 3D FEA solution also solves for stress throughout the whole shell, not just at one point. However, the 3D FEA solution will be biased if the material properties of the brass do not perfectly replicate reality. Additionally, the 3D FEA solution does pose unique challenges in terms of error analysis.

3.6.2.5 Error and Sensitivity Analysis

Due to calculation times for 3D FEA solutions (Table 4.1), a Monte Carlo simulation is not practical. Additionally, the delta method cannot be performed because the FEA solver is an analytic “black box” as far as this method is concerned. Thus, the only method available for propagating error through the FEA solver is the AMV+ method. This can be done either manually or automated by NESSUS. While the automated process is preferred, NESSUS is Windows based software and cannot be run on CentOS machines, such as supercomputers. This leaves two compromise options: manual AMV+ on a fast supercomputer and automated AMV+ on a slower personal computer. The manual AMV+ method will not produce sensitivity data, but NESSUS automatically provides sensitivity analysis outputs for any AMV+ solution. Beyond intuition, that is the only sensitivity analysis information available for the 3D FEA model. Thus, NESSUS will be used to automate the AMV+ solution.

3.6.2.6 Shell Stress Distribution

All previous numerical analysis described produces a single value for stress (analytic σ_t and FEA σ_{pS}). To understand the test, more needs to be known about stress at different locations. Fortunately, Abaqus is able to display the interpolated stress along a path. The

path chosen for visualizing stress on the inner surface of the shell is shown in Figure 3.8.

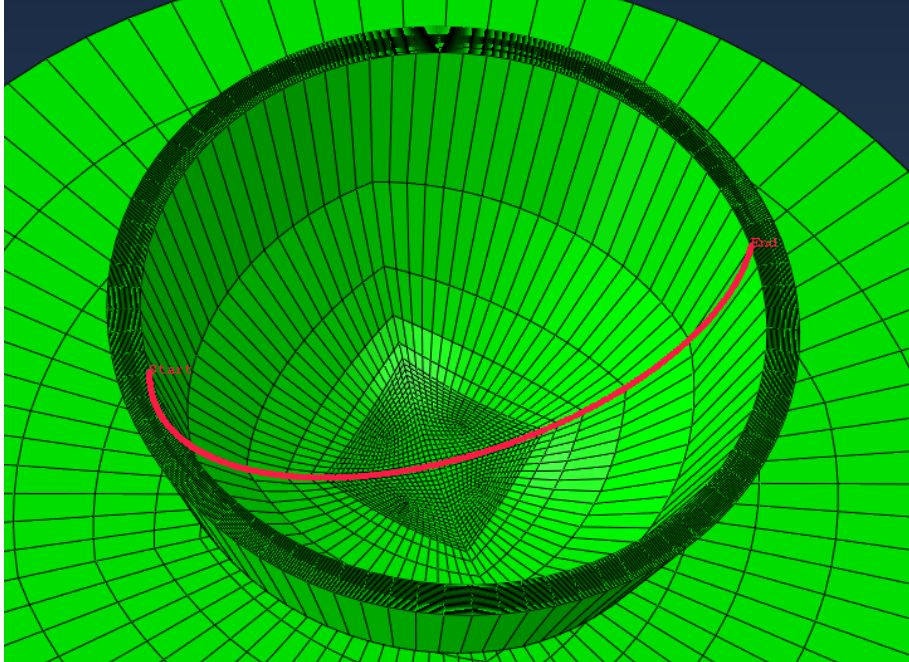


Figure 3.8: Circumferential FEA Results Path on Inner Surface of Shell

This path is similar to one used in existing published research, therefore it facilitates comparison to previous results (Figure 2.2)[13]. As in previous research, these results can be used to verify whether or not the analytic solution is an acceptable approximation for fracture strength. They can also be used to show both stress and area stressed for use in Weibull calculations. Finally, these results can ultimately be used to define best practices for creating fracture-inducing stress states closest to those experienced in-service (equi-biaxial stress).

3.6.3 Weibull Distribution Calculations

Use of the Weibull distribution in ceramic mechanical failures is well documented and there is even an ASTM standard for its application to uniaxial strength data [26]. Calculations in the specific case of diametrical compression testing of TRISO SiC shells has also been established by previous researchers. The following methodology has been modified from recent TRISO-specific publications [5][17]. Equation (3.26) defines the CDF of the Weibull two-parameter distribution [27].

$$F(x; \lambda, k) = 1 - \exp \left[- \left(\frac{x}{\lambda} \right)^k \right] \quad (3.26)$$

Where:

λ = Scale Parameter

k = Shape Parameter

In the case of ceramics fracture mechanics, “ x ” is the fracture stress (σ_f), the scale parameter (λ) is the characteristic strength (σ_0), and the shape parameter (k) is the Weibull modulus (m). Substituting these values into the CDF results in Equation (3.27), which is a modified version of recently published equations [5][17].

$$P = 1 - \exp \left[- \left(\frac{\sigma_f}{\sigma_0} \right)^m \right] \quad (3.27)$$

Where:

P = Probability that Sample Strength is $< \sigma_f$

σ_f = Fracture Stress

σ_0 = Characteristic Strength

m = Weibull Modulus

The values of σ_f are unique for each test article and are determined by the analytic and/or FEA solution. It represents a uniform stress state acting on an inner surface area of the shell at fracture. In actuality, the stress state varies with position and is not uniform. Thus, later work herein will propose ways in which to convert the varying stress state to one that is more accurately approximated.

In terms of visualizing the Weibull distribution, Equation (3.28) shows a form of Equation (3.27) which produces a linear plot where m is the slope and σ_0 is determined by the intercept point.

$$\ln \left[\ln \left(\frac{1}{1-P} \right) \right] = m \cdot \ln(\sigma_f) + \ln \left(\frac{1}{\sigma_0^m} \right) \quad (3.28)$$

There are multiple data points and the Weibull plot is effectively a linear curve fit to the data set. The values of σ_f are sorted in ascending order and expressed as indexed σ_i values. A conservative cumulative probability of failure (P_i) for the i^{th} ranked stress is defined by Equation (3.29) [5][17].

$$P_i = \frac{i}{N+1} \quad (3.29)$$

Thus, σ_0 and m can be determined from the empirical data for σ_f . The value of σ_0 is related to the mean of the distribution. In the CDF, $\sim 63.2\%$ of a sample population will exhibit a characteristic strength less than σ_0 .

In practice, this method is implemented manually through a linear curve fit of Equation (3.28). Additionally, the built-in MATLAB function “wblfit” will be used with σ_f to obtain the maximum likelihood estimators for Weibull distribution parameters σ_0 and m . Thus, all parameters in Equations (3.27) - (3.29) are known and then results can be scaled to different size surface areas. The scaling of σ_0 is described in a previous publication:

The effective surface can be used to scale ceramic strengths from one component size to another or from one loading configuration to another. This accounts for the increased probability that larger specimens possess more critical flaws. For two specimens having different sizes or loading configurations, the ratio between their mean fracture strengths (or characteristic strengths) can be correlated with the ratio of the effective surface areas. [17]

Scaling is shown in Equation (3.30), where the superscripts represent the locally stressed section of the test article (L) and the full SiC shell used in service (F).

$$\frac{\sigma_0^F}{\sigma_0^L} = \left(\frac{S_E^L}{S_E^F} \right)^{1/m} \quad (3.30)$$

For the analytic solution, the mean cross-sectional divot area and the mean total inner surface area can be substituted into Equation (3.30) to produce Equation (3.31).

$$\sigma_0^F = \sigma_0^L \cdot \left(\frac{\pi \bar{r}_0^2}{4\pi (\bar{R}_2 - \bar{t})^2} \right)^{1/m} \quad (3.31)$$

Thus, σ_0^F and m are defined for the full shell. These results can be compared to other published results for TRISO SiC shell strength. However, this uses one value of S_E^L for an entire population even though the divot radius is different for each test article. Thus, an additionally modified method must be developed.

It is possible to iteratively determine the parameters of the Weibull distribution for the full shell if the scaling in Equation (3.30) is used before the curve fit in Equation (3.28). In this case, Equation (3.30) is modified so that σ_{fi}^F is determined for the i^{th} individual test article. The result is Equation (3.32).

$$\sigma_{fi}^F = \sigma_{fi}^L \cdot \left(\frac{\pi r_{0i}^2}{4\pi (\bar{R}_2 - \bar{t})^2} \right)^{1/m} \quad (3.32)$$

For the first iteration of this method, an initial m is chosen ($m_0 = 3.5$). Values of σ_{fi}^F are then ranked in ascending order and Equation (3.29) determines P_i values. To finish an iteration, a linear curve fit of Equation (3.33) is performed.

$$\ln \left[\ln \left(\frac{1}{1-P} \right) \right] = m \cdot \ln (\sigma_f^F) + \ln \left(\frac{1}{(\sigma_0^F)^m} \right) \quad (3.33)$$

At this point, σ_0^F and m are known. The new value of m is plugged into Equation (3.32) and another iteration is performed. In practice, this method has short calculation times and easily converges within $\epsilon = 0.01$. Ultimately, the iterative method is more accurate because it matches individual stress states with their respective divot sizes. It will also be shown to be more conservative and thus the final results for σ_0^F and m will be determined by the iterative method.

For future work, it is important to note that these results are expressed as a probability distribution. Thus, safety factors are not necessarily the best way to control failures. Since

probabilities are native to the solution it is easy to determine a value of σ_f in which 99.9% of a sample population will have a fracture strength greater than σ_f . In this way, failures in-service can be controlled.

CHAPTER 4

RESULTS AND DISCUSSION

The diametrical compression of SiC hemispheres is a unique test and it is not performed in accordance with a well established standard (e.g. a charpy test). Hence, before a large population of samples can be effectively tested, the test itself must first be characterized. After all numerical methods are fixed and the solid mechanics of the test are thoroughly understood, testing of SiC hemispheres can be conducted with confidence in the accuracy and precision of the results. Finally, the results of the test can be compared to other researcher's published data and conclusions can be made.

4.1 Primary Test Article Failure Mechanism

From viewing the pieces of crushed samples it can be qualitatively determined that fracture initiates near the apex of the hemisphere (Figure 4.1)[5]. This occurs when a local maximum principal stress (σ_{p1}) exceeds the material strength at the location of a critical flaw. After initiation, cracks rapidly propagate through the SiC shell and the test article experiences mechanical failure.

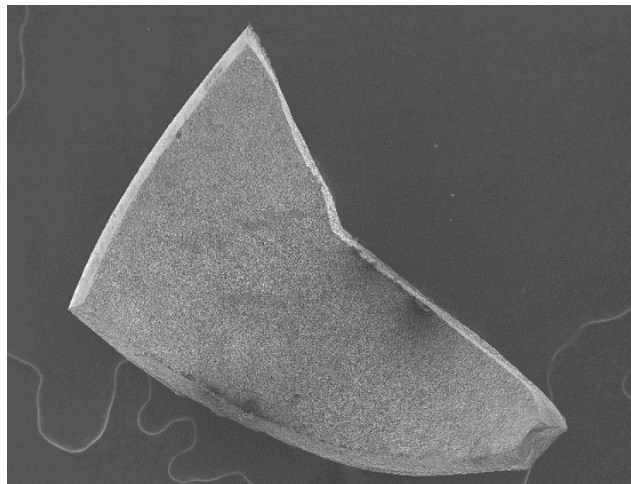


Figure 4.1: SiC Shell Piece Created by Fracture Initiation near Hemisphere Apex

This is the primary failure mechanism and the only one which garners interest in developing a controlled test that produces precise data. The analytic solution result of σ_t is at the exact apex on the inner surface of the hemisphere. The 3D FEA solution solves σ_{p1} at all locations and returns σ_{pS} for the entire model. Unlike the analytic solution, σ_{pS} is not necessarily at the inner-apex.

4.2 3D Finite Element Analysis Convergence Study

Before FEA models can be employed, a convergence study must first be performed. The validation of any FEA solution is a convergence study where element discretization is refined until change in output is reduced below an arbitrary tolerance (ϵ). Shown in Figure 4.2 are results from an intermediate convergence study where shell elements are changed while the indenter discretization is held constant. Figure 4.3 shows results where indenter elements change and the shell discretization is held constant. For each step, only one discretization parameter is changed. The goal is to understand the general effect that individual parameters have on the two main results: σ_{pS} and F_R . (Tabular Data: Table A.1)

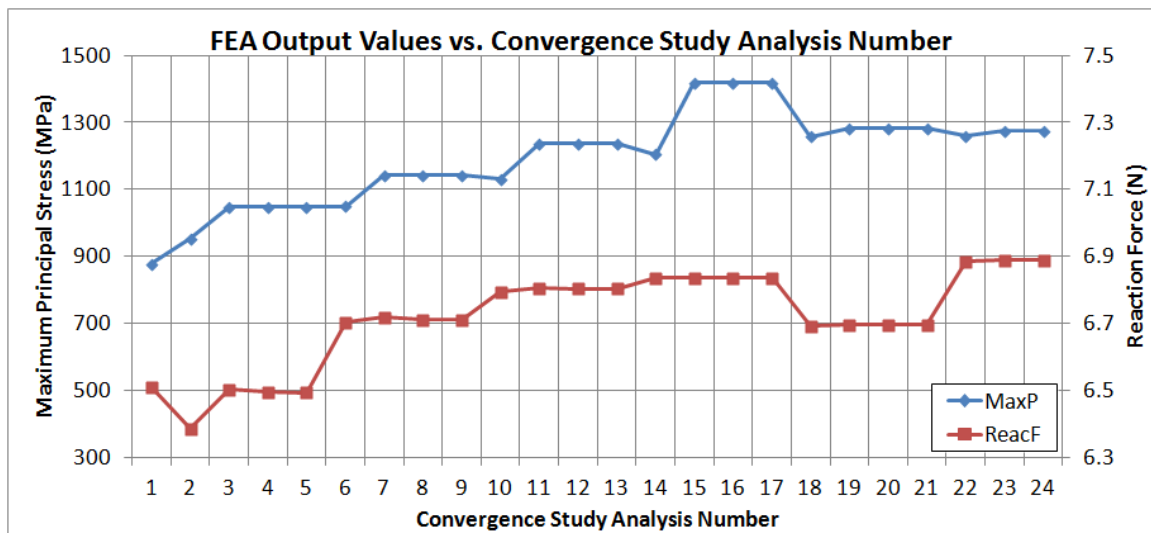


Figure 4.2: FEA Convergence with Changes in Shell Discretization

For the study in Figure 4.2, several model characteristics can be noted from the results of specific analysis numbers:

1. (6–7 & 10–11) The largest rises in stress occur when the number of elements in the shell thickness are increased.
2. (7–9 & 11–13) Increases in the number of radial elements and bias have no effect on the results, suggesting only geometry local to the contact area is important.
3. (9–10 & 13–14) Rises in reaction force and drops in stress occur when increasing the number of circumferential elements, suggesting that this element refinement results in a higher but more evenly distributed force.
4. (15–17 & 18–21) The model is subject to false highs and lows in both stress and reaction force. This is possibly created by changes in how element boundaries line up and contact overclosure is calculated.

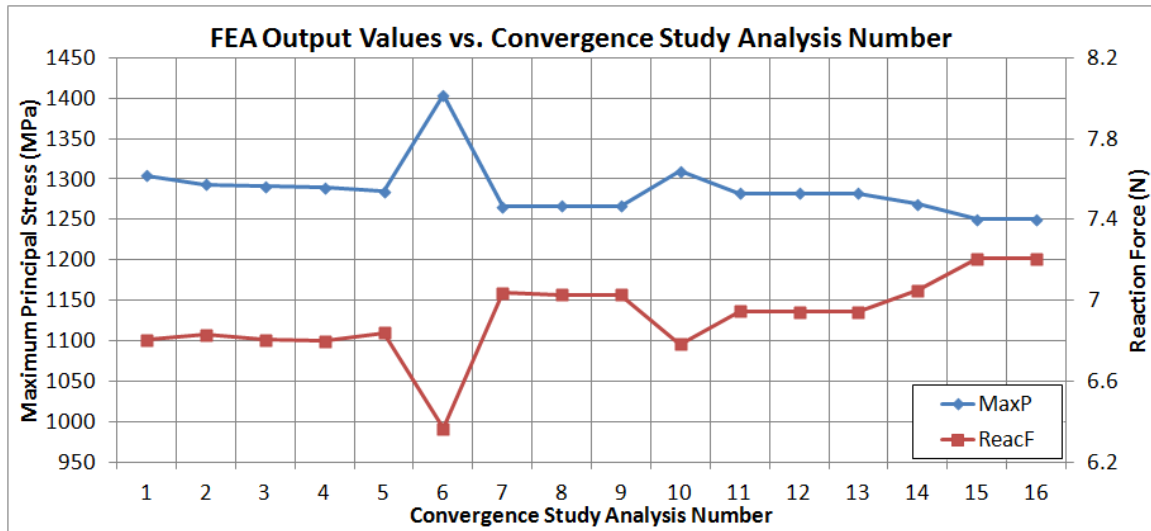


Figure 4.3: FEA Convergence with Changes in Indenter Discretization

For the study in Figure 4.3, several model characteristics can be noted from the results of specific analysis numbers:

1. (6 & 10) The spikes in stress and force occur when the number of circumferential elements is increased and results return to normal after the number of thickness elements is increased, suggesting that this is an aspect ratio induced outlier.

2. (7–9 & 11–13) Again, increases in the number of radial elements and bias have essentially no effect on the results.
3. (1–16) As the elements in the indenter are increased, force increases and stress decreases, suggesting that a higher resolution contact area creates a larger force that is more evenly distributed.

With the knowledge gained from the intermediate convergence studies, a more concise and effective main convergence study can be performed. It will utilize the following considerations and parameters: circumferential elements in the shell and indenter will be the same at higher resolutions, preventing outliers created by element mismatch in the contact area; the number of thickness elements will be adjusted with the number of circumferential elements so that general aspect ratios are maintained at each step; radial elements and their bias will not be increased as they increase computational cost without improvements in accuracy.

Shown in Figure 4.4 and Table 4.1 are the abbreviated results of the main convergence study for linear elements in both shell and indenter. (Tabular Data: Table A.2)

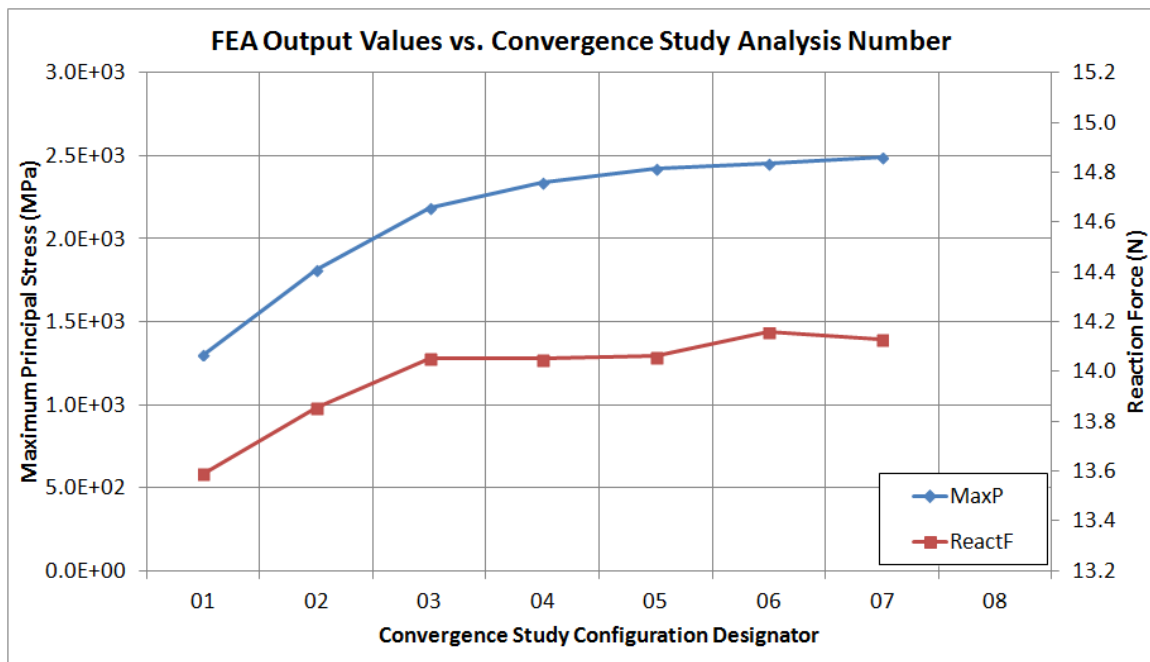


Figure 4.4: Main FEA Convergence Study

Table 4.1: Selected Main FEA Convergence Study Configuration Results

Name	Wall Time (hr)	$\sigma_{pS}(MPa)$	$\Delta\sigma_{pS}(\%)$	$F_R(N)$	$\Delta F_R(\%)$
05	2.5	2422	3.54%	14.06	0.08%
06	11.5	2455	1.39%	14.16	0.69%
07	26.9	2490	1.41%	14.13	0.21%

The three configurations post-convergence ($\epsilon=0.05$) are “05”, “06”, and “07”. Due to calculation times, “07” is not the only option for solving the model. If an analysis task can accept an additional error of $\sim 3\%$ in σ_{pS} , the “05” analysis can be run approximately ten times in the duration it would take to get one “07” result. The analysis reported herein can sacrifice that accuracy for a benefit in calculation time.

Additionally, there are other results worth noting: the “05” model has 32,000 and 84,000 linear elements in the shell and indenter, respectively; in a typical model the maximum brass indenter strain is ~ 0.05 ; for visualization, an exaggerated deformed shell showing the localized nature of test article response is shown in Figure 4.5.

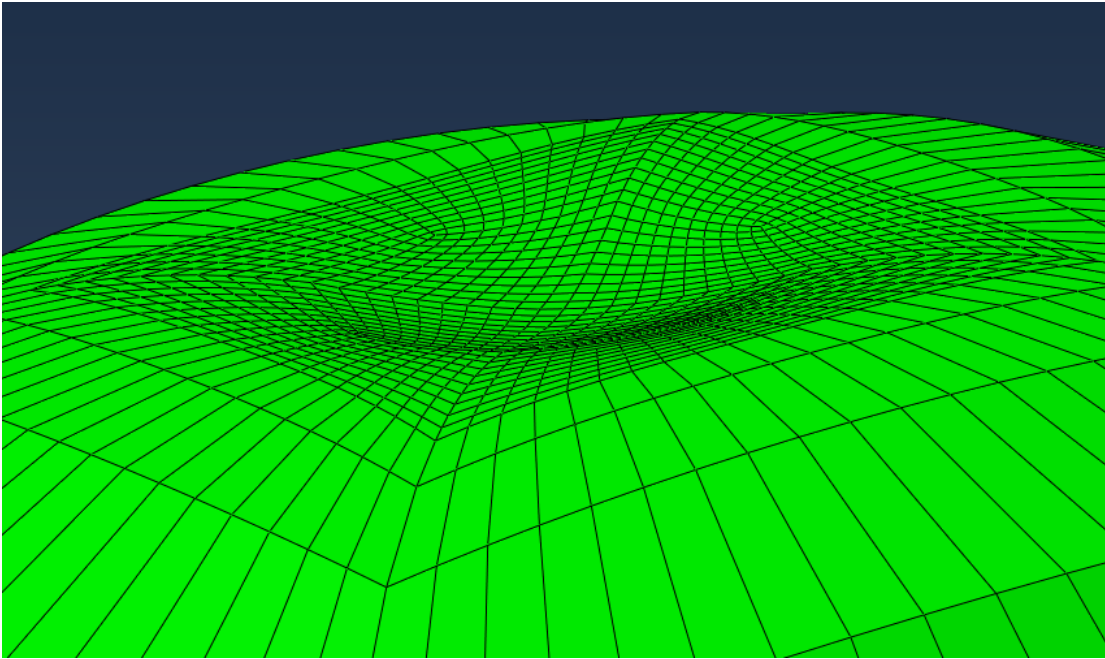


Figure 4.5: Exaggerated Deformed Shape of “05” Convergence Study Model

Furthermore, the following Abaqus options were finalized: nlgeom, no; unsym, no; element type, linear; contact type, surface to surface. With nonlinear geometry turned off, it is assumed that element discretization is refined enough for linear approximations to effectively represent deformed shapes.

4.3 Test and Analysis Characterization

This application-specific test and the associated numerical analyses must be characterized because a well defined standard does not exist. However, numerous milestones achieved by previous researchers are shown in the literature review and methodology sections. Thus, the test and analysis characterization is not an entirely blind operation. Instead, it builds upon the work of previous researchers, creating a value added step in the continuous improvement process.

4.3.1 Empirical Average Geometry Data

Diametrical compression tests were performed on two separate sets of test articles: 6 and 9 shells were fractured by a nickel and brass crush plate, respectively. The discrete data points, truncated well beyond reasonable significant figures, are located in Table A.5. While not every value is an exact arithmetic mean of the population, Table 4.2 contains input data for an “average” test article.

Table 4.2: Test Characterization Input Data (Average Geometry)

SN	$P(N)$	δP	$r_0(\mu m)$	δr_0	ν	$\delta \nu$	$t(\mu m)$	δt	$R_2(\mu m)$	δR_2
BrAv01	11.00	0.11	70.0	3.5	0.21	0.0021	37.1	1.7	398	8

Average geometry, material constants, and varying force were used to characterize the shell stress state by means of solution techniques defined in the methodology.

4.3.2 Initial Analytic Solution Linearly Interpolated Curves

Before viewing analytic solution results for empirical data, it is important to understand the effects of P and r_0 on σ_t . Plotted in Figure 4.6 are analytic solution results for σ_t vs. P when r_0 is held constant and σ_t vs. r_0 when P is held constant.

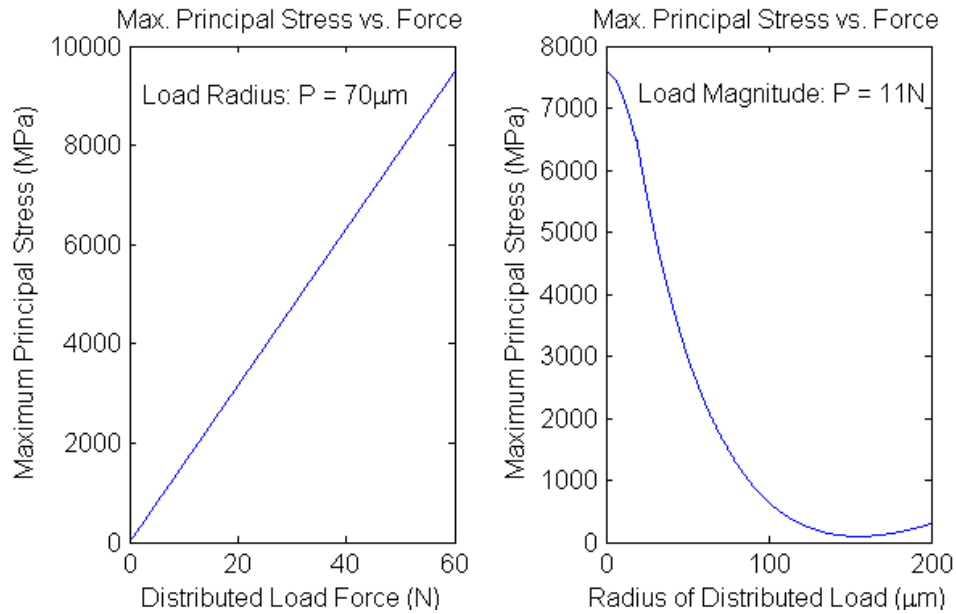


Figure 4.6: Stress vs. Load and Divot Size for the Analytic Solution

It is clear that σ_t increases with P , but decreases with r_0 . However, in actual test conditions neither variable is constant. When considering the crush plate material as the test article and the shell as an indenter, the test functions as a hardness test. Thus, the Brinell hardness equation can be temporarily used to define the relationship of r_0 vs. P to create a plot for σ_t vs. P . Shown in Figure 4.7, this plot is instrumental in understanding the diametrical compression test. (*Note: This is only for reference because testing is performed outside the range of the Brinell hardness scale.*)

With the Brinell hardness values representing the differences between generic crush plate materials, there are several observations that can be made about Figure 4.7:

1. For any given crush plate material there is a maximum value of σ_t that can be induced in the shell through the primary failure mechanism (first peak).

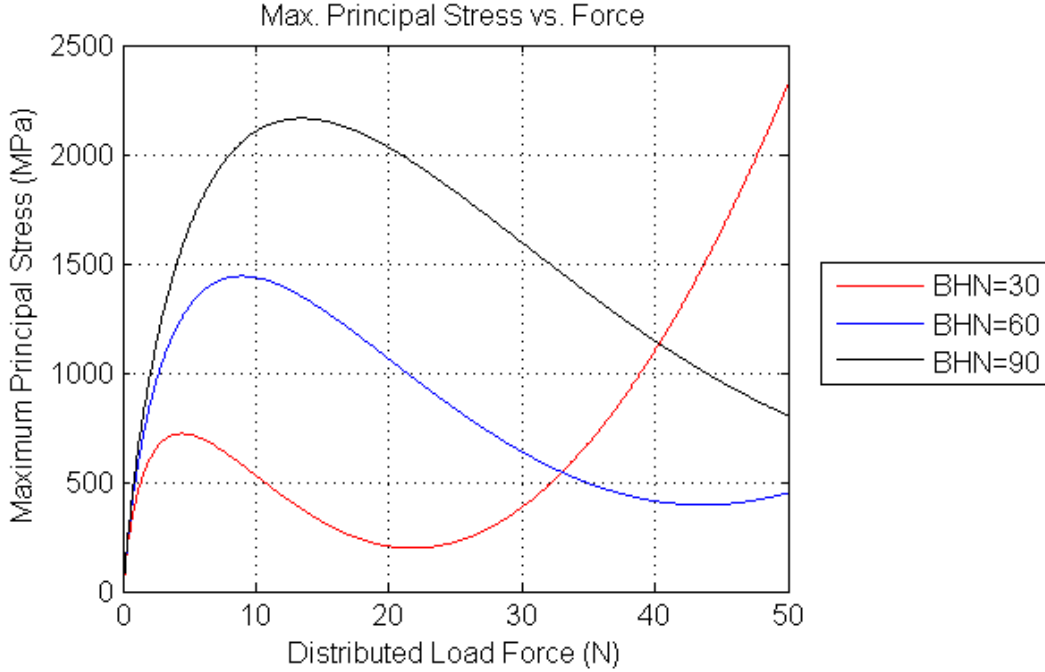


Figure 4.7: Analytic Solution σ_t vs. P for Different BHN Materials (Reference Only)

2. The second rise in the curve is beyond testing loads and appears indicative of a secondary failure mechanism not applicable to tests performed in this research.
3. Some materials will not fracture an SiC shell through the primary failure mechanism because they are too soft to produce enough stress (e.g. the BHN=30 curve peaks at 750MPa and should not consistently fracture test articles).
4. Experimental results are not expected to contain many fractures on the declining side of the peak as this represents a failure at a previously survived stress.

While the curves in Figure 4.7 are acceptable for reference purposes, they must be revised with a more valid relationship between r_0 vs. P . This relationship was determined with FEA because instantaneous r_0 is not recorded during empirical testing.

4.3.3 FEA Solution Linearly Interpolated Curves

The same FEA model that can be used to determine σ_{pS} vs. F_R (analytic equivalent: σ_t vs. P), can first be used to determine the relationship between r_d vs. F_R (analytic equivalent:

r_0 vs. P). The FEA model requires a true stress vs. true plastic strain curve for the indenter material. This has been experimentally generated for the brass and the following results are only valid for brass crush plate tests.

Initial FEA tests which created 12 different divot sizes in the indenter material were performed. Reaction force (F_R) in the final frame was queried by a Python script and the divot radius (r_d) was measured with a manual distance query in the GUI (Graphical User Interface). The resulting relationship of r_d vs. F_R and a MATLAB power law curve fit are shown in Figure 4.8. (Tabular Data: Table A.3)

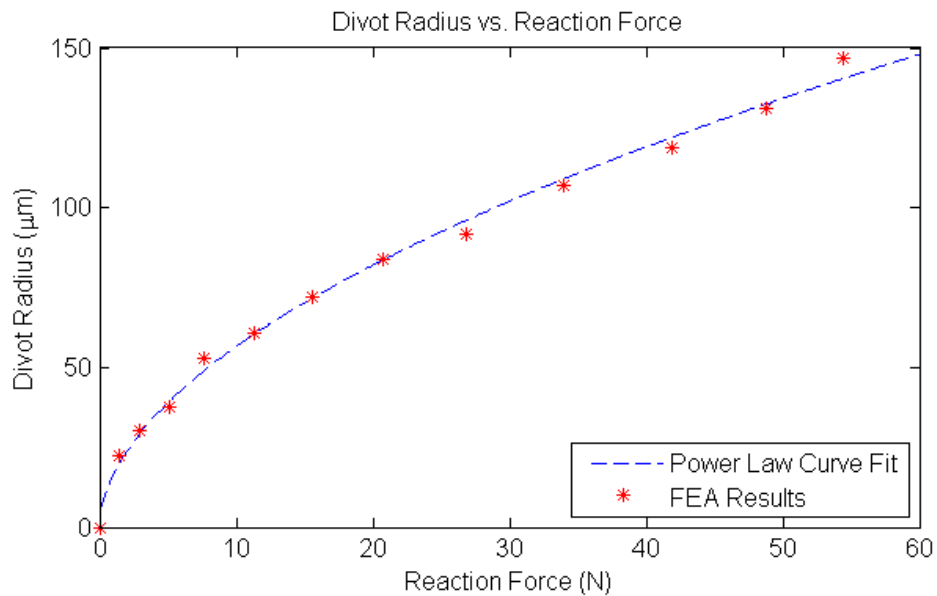


Figure 4.8: FEA Data Points and Power Law Curve Fit for r_d vs. F_R

For the power law curve fit previously defined in Equation (3.15) and shown in Figure 4.8, the analytic solution has a more valid r_0 vs. P which results in a more valid σ_t vs. P . The next logical step is to compare the two solution methods by plotting σ_{pS} vs. F_R (FEA result) and σ_t vs. P (analytic result) together.

4.3.4 Multiple Solution Linearly Interpolated Curves

Up to this point, the FEA model and analytic solution for stress have been performed in parallel. Currently, only the pseudo-hardness of the indenter has been matched between

the two methods (r_0 vs. P is a curve fit of r_d vs. F_R). Assuming the maximum stress is located at the inner-apex, both methods should produce similar results for stress vs. force (i.e. FEA: σ_{pS} vs. F_R , Analytic: σ_t vs. P). Shown in Figure 4.9 are the linearly interpolated curve results. (Tabular Data: Table A.3)

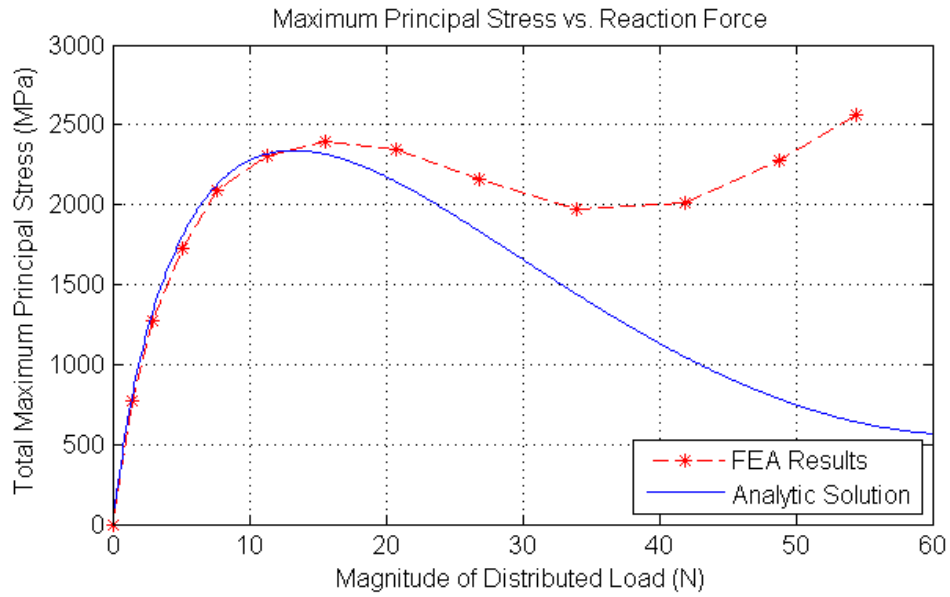


Figure 4.9: FEA and Analytic Solution Linearly Interpolated Stress vs. Force

There are several characteristics which are evident from Figure 4.9:

1. The two solutions are nearly identical until the peak in the stress curve.
2. The FEA solution peaks slightly higher and later than the analytic solution.
3. After the peak, the FEA and analytic solution diverge significantly.
4. The second rise in the FEA solution is indicative of a secondary failure mechanism (similar to the analytic solution in Figure 4.7).

While the curve section before the peak validates both parallel methods, the divergence must be investigated. As previously stated, the analytic solution solves for the maximum principal stress at the inner-apex, while the FEA model solves for the supremum principal stress over

the entire shell. Thus, the best way to understand the divergence between the two solutions is to plot the FEA stress profile on the inner shell surface (Figure 3.8).

4.3.5 Maximum Principal Stress Profile on Inner Shell Surface

Abaqus has the ability to plot results along a predefined path. While these plots do contain interpolated values at locations between integration points, the overall purpose is to view the shape and magnitude of maximum principal stress (σ_{p1}) along the path, not to fixate on a single result at an integration point. Shown below in Figure 4.10 are the σ_{p1} vs. y results for the same models used to create Figure 4.8 and Figure 4.9.

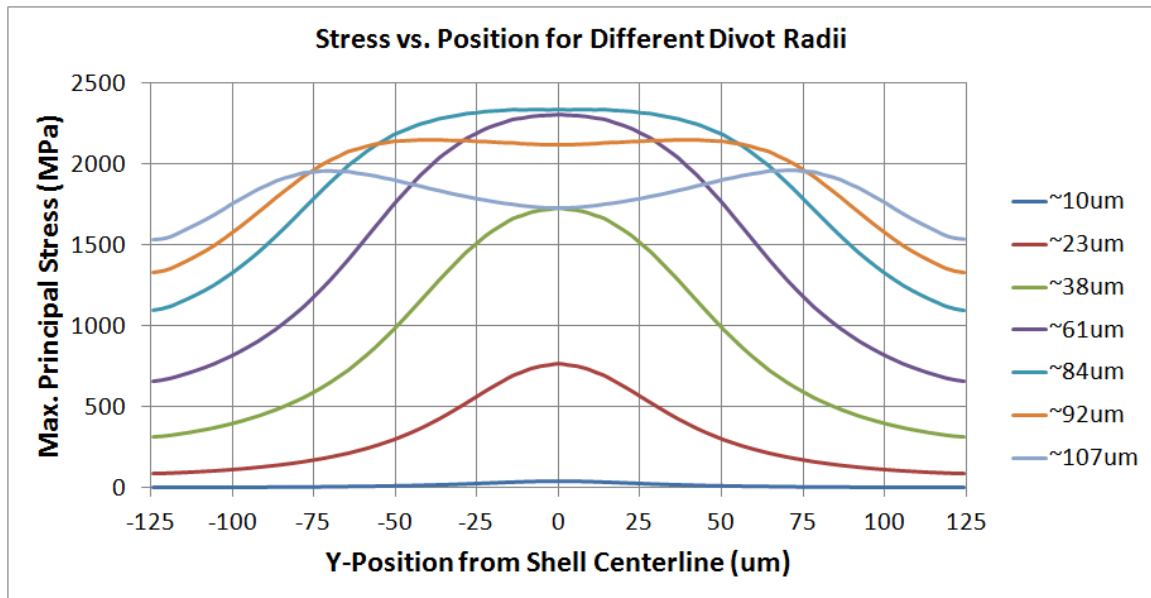


Figure 4.10: Maximum Principal Stress (σ_{p1}) Profile for Multiple Divot Sizes

Several key characteristics can be noted from the results in Figure 4.10.

1. For smaller divot sizes ($r_d < \sim 80\mu m$), σ_{pS} is located at the inner-apex, the same location as the analytic solution.
2. At a transition in the stress pattern ($r_d \sim 84\mu m$), σ_{pS} stops increasing in magnitude and begins increasing the area it affects. This is at the same divot size where the peak in σ_{pS} vs. F_R can be seen in Figure 4.9.

3. After this transition ($r_d > \sim 85\mu m$) σ_{pS} is located at two points symmetric about the inner-apex. Thus, σ_{pS} is not located at the inner-apex and the FEA and analytic solutions will have different results. This explains the diverging curves in Figure 4.9. It also shows that the analytic solution is no longer valid in determining σ_{pS} after the transition. (Note: the “two points” of σ_{pS} in Figure 4.10 actually represent a “halo” of σ_{pS} around the inner-apex of the shell.)
4. The stress profile published in previous research (Figure 2.2) is similar to the profile in Figure 4.10 for $r_d \sim 107\mu m$ [13]. It is important to note that this general stress pattern is only valid for one small range of divot sizes.

In addition to plotting σ_{p1} vs. y , all three principal stresses ($\sigma_{p1}, \sigma_{p2}, \sigma_{p3}$) can be plotted for one value of r_d . An example of this plot is shown in Figure 4.11.

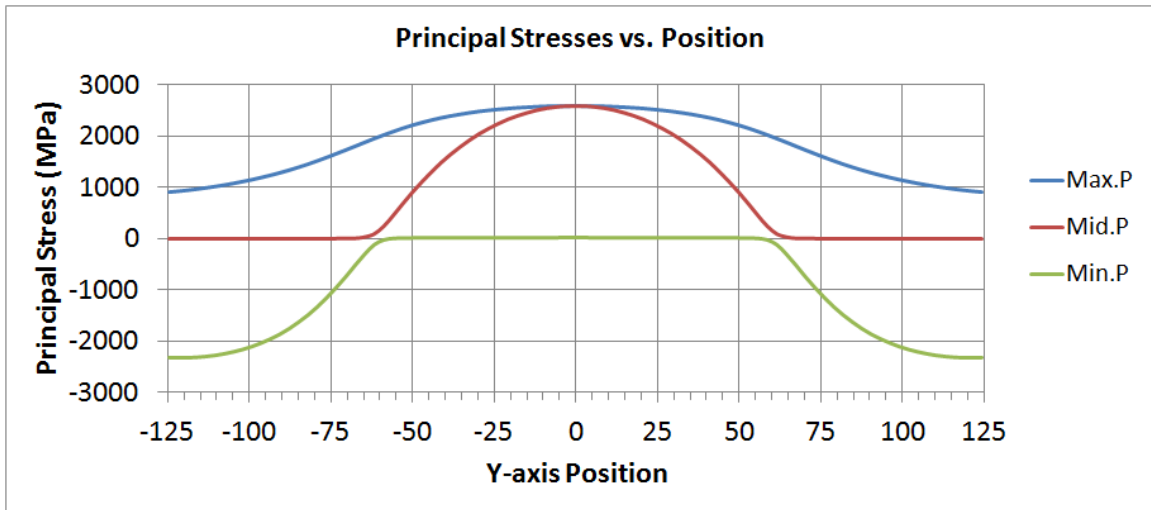


Figure 4.11: Principal Stresses ($\sigma_{p1}, \sigma_{p2}, \sigma_{p3}$) Profile (Reference Only)

The most important characteristic illustrated by Figure 4.11 is the existence of equi-biaxial stress only at the inner-apex. Moving away from this point, the stress state becomes less equi-biaxial and hoop stress in one direction becomes more dominant.

During operational and emergency conditions in a nuclear power plant, the SiC shell functions as a spherical pressure vessel. If it is considered to be ideally spherical, there is

equi-biaxial stress at every point on the inner surface. During a diametrical compression test, the stress state at the inner-apex best replicates in-service conditions. Thus, the test should be designed so that the divot size is at or below the transition threshold shown in Figure 4.9, σ_{pS} is located at the inner-apex of the shell, and an equi-biaxial stress state is created there ($\sigma_{pS} = \sigma_{p1} = \sigma_{p2}$).

4.3.6 Critical Maximum Principal Stress

As noted by previous researchers, the area under the divot conservatively envelops the highest value of maximum principal stress [5]. Shown in Figure 4.12 are three profiles from Figure 4.10, except the range of data is limited to the divot radius. Additionally, Figure 4.12 also shows the results of the analytic solution, which are individual data points located at the inner-apex.

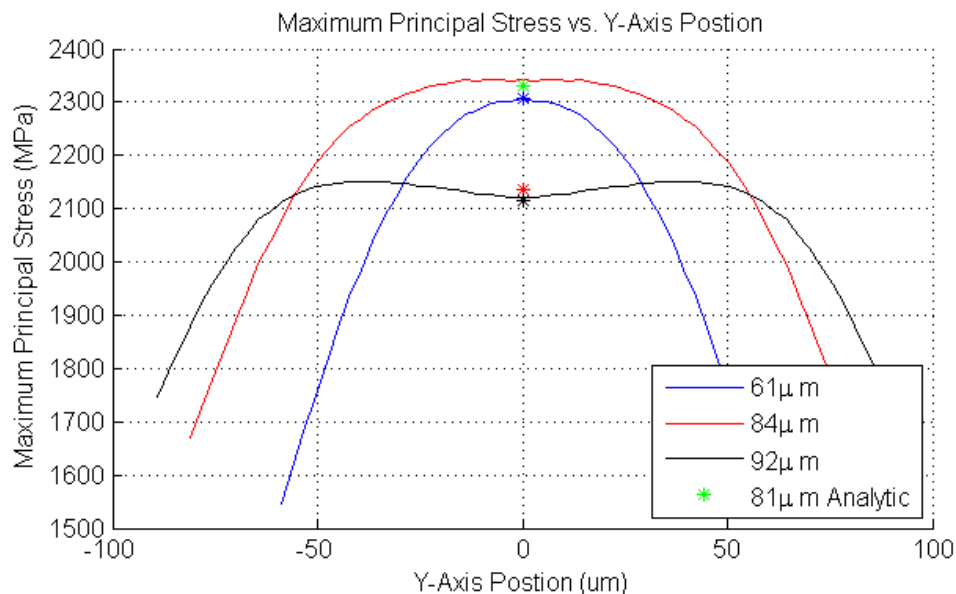


Figure 4.12: Maximum Principal Stress (σ_{p1}) Profile Under Divot Area

In two of three cases, the analytic solution qualitatively matches the FEA results for σ_{p1} at the inner-apex. For $r_d \sim 84\mu m$ the two methods do not match. However, Figure 4.12 also shows a matching analytic solution result where divot radius has been changed from $\sim 84\mu m$ to $\sim 81\mu m$ ($\sim 3.5\%$). Thus, the solutions do produce similar results, but are hyper-sensitive

to changes in divot radius. Concerning the local stress profile, other researchers have stated:

For the majority of the inner surface area just below the loading contact area, the stress variation is less than 10% of maximum stress, which justifies the use of the loading contact area for the effective area. [5]

This comes from the same research as Figure 2.2, which has been related to the $r_d \sim 107\mu m$ stress pattern. While the statement is valid for their data, it is not valid for all divot sizes and should not be used as a general rule. Shown in Table 4.3 are the bounds of σ_{p1} under the divot.

Table 4.3: Min. & Max. Stress Profile Values Under Divot

$\sim r_d$	Min. σ_{p1}	Max. σ_{p1}	% Difference
61	1545	2307	33.0
84	1665	2342	28.9
92	1747	2152	18.8

The wide range of σ_{p1} in Figure 4.10 and Table 4.3 shows why a finalized Weibull statistical analysis should not simply use the analytic solution results of $\sigma_f = \sigma_{p1}$ and $S_E^L = \pi r_0^2$. A more accurate and conservative method is shown in the “Multi-Method Conservative Weibull Distribution” subsection.

4.4 Error and Sensitivity Characterization

Results in the previous section have come from analyses which are focused on producing deterministic solutions. Additionally, it is important to characterize error in the solutions and understand sensitivity to changes in input variables. Thus, detailed results will be presented concerning quantifiable errors calculated through traditional means, while sensitivity factors will be presented and discussed in relative terms. Finally, non-quantifiable errors are discussed from a qualitative perspective. Because errors are not propagated through the Weibull distribution calculations, the overall purpose of these results is to better understand

the validity of the analytic and FEA solutions in light of the unavoidable experimental errors introduced in testing.

4.4.1 Analytic Solution Quantitative Error

Three different techniques are used to characterize error in the analytic solution: Monte Carlo, AMV+, and the delta method. In this initial comparison, error created by divot size and/or asphericity (δr_0) is held constant at 5%. Parameters are taken from an averaged brass crush plate test sample (BrAv01, Table 4.2). The first two methods are evaluated for σ_t at 15.9%, 50%, and 84.1% probability in the CDF (i.e. the equivalent of $\sigma_t \pm \delta\sigma_t$ in the delta method).

Any Monte Carlo simulation needs to go through a convergence study where the varying parameter is the number of samples in the simulation. Shown in Table 4.4 is a convergence study which ranges from 5×10^1 to 5×10^6 samples.

Table 4.4: Monte Carlo Error Analysis Convergence Study

Samples N	CDF Probability of σ_t			Percent Difference in Step		
	15.9%	50%	84.1%	15.9%	50%	84.1%
5.0E+01	1566.0	1713.3	1876.9			
5.0E+02	1546.9	1728.4	1941.7	-1.217%	0.880%	3.449%
5.0E+03	1547.4	1734.1	1943.1	0.031%	0.332%	0.072%
5.0E+04	1548.0	1736.5	1945.6	0.040%	0.139%	0.132%
5.0E+05	1548.8	1735.5	1945.5	0.050%	-0.059%	-0.007%
5.0E+06	1549.5	1736.1	1945.7	0.046%	0.033%	0.014%

Table 4.4 shows that the simulation converges with $\epsilon = 0.001$ (i.e. 0.1%) at a sample size of 5×10^5 . This is acceptable for repeated calculations if the Monte Carlo method is used to determine error for each test article. However, the results of the 5×10^6 simulation are considered to be more accurate than any other method and its results will be used for the single sample comparison in Table 4.5.

The AMV+ method is a less prolific technique, but it is well established and reference material which outlines it's manual implementation is available [24]. In this study, the method is automated using NESSUS statistical software [25]. The delta method is implemented using Equations (3.16) - (3.19) in Mathematica and MATLAB. The results of all three methods are compared in Table 4.5.

Table 4.5: Comparison of Different Error Propagation Techniques ($\delta r_0 = 5\%$)

Sample Number	CDF Probability of σ_t			Percent Difference from MC		
Method	15.9%	50%	84.1%	15.9%	50%	84.1%
BrAv01						
MC 5e6	1549.5	1736.1	1945.7			
AMV+	1551.7	1738.7	1948.6	0.15%	0.15%	0.15%
Mathematica	1540.8	1738.7	1936.5	-0.56%	0.15%	-0.47%
MATLAB	1540.8	1738.7	1936.6	-0.56%	0.15%	-0.47%
MathCAD		1738.7			0.15%	

First, the deterministic solution deviates from the Monte Carlo simulation by 0.15%. It is known that the deterministic solution does not give the exact statistical “expected value” for σ_t . This confirms that the bias of the delta method is $< 0.1\%$ for this test article. Concerning error values, not one result deviates from the Monte Carlo results by more than $\sim 0.5\%$. All deviations are small enough and thus any method is acceptable. Due to simplicity of implementation in MATLAB, the deterministic solution and delta method will be used to determine $\sigma_t \pm \delta\sigma_t$ for all empirical data.

4.4.2 Analytic Solution Input Variable Sensitivity

There are several methods which can be used to quantify output sensitivity with respect to input variables and their errors. One of the simplest methods is to compare the values for each term under the square root in the delta method Equation (3.16). Located in Table 4.6, this effectively shows the sensitivity of output error to input error. (Note: input values are the same as those used to create Table 4.5.)

Table 4.6: Sensitivity of Analytic Solution Error to Input Errors

$\left(\frac{\partial\sigma_t}{\partial r_0}\right)^2(\delta r_0)^2$	$\left(\frac{\partial\sigma_t}{\partial P}\right)^2(\delta P)^2$	$\left(\frac{\partial\sigma_t}{\partial\nu}\right)^2(\delta\nu)^2$	$\left(\frac{\partial\sigma_t}{\partial R_2}\right)^2(\delta R_2)^2$	$\left(\frac{\partial\sigma_t}{\partial t}\right)^2(\delta t)^2$
3.1439e16 Pa ²	3.0230e14 Pa ²	4.4501e13 Pa ²	1.2787e15 Pa ²	6.0985e15 Pa ²

Due to scale, the most important aspects in Table 4.6 are the orders of magnitude. It is clear that r_0 , with 5% error, is the dominant term. The two shell geometry values, t and R_2 , are the next most influential. Finally, P and ν are the least important. While one would expect P to be more important, it is not. Thus, the divot radius r_0 has been shown to be the most important factor in determining analytic solution error.

If the error values are removed from the equation, just leaving the partial derivatives evaluated at the means of the input values, then the results become a basic sensitivity analysis. Located in Table 4.7, this effectively shows the sensitivity of the deterministic solution to nominal input values.

Table 4.7: Sensitivity of Analytic Solution to Input Values

$\left(\frac{\partial\sigma_t}{\partial r_0}\right)$	$\left(\frac{\partial\sigma_t}{\partial P}\right)$	$\left(\frac{\partial\sigma_t}{\partial\nu}\right)$	$\left(\frac{\partial\sigma_t}{\partial R_2}\right)$	$\left(\frac{\partial\sigma_t}{\partial t}\right)$
-5.066e13 $\left(\frac{Pa}{m}\right)$	1.581e8 $\left(\frac{Pa}{N}\right)$	3.177e9 (Pa)	4.47e12 $\left(\frac{Pa}{m}\right)$	-4.594e13 $\left(\frac{Pa}{m}\right)$

The first thing to recognize about Table 4.7 is that the units are not uniform. Still, there is a similar pattern: r_0 is the largest, followed by shell geometry values t and R_2 , with ν and P being least important. In the case of this open-ended solution, redundancy in results provides greater assurance to their validity.

It is important to note that Table 4.6 and Table 4.7 show results at specific input values. These results change based on the input values used because the analytic solution is not linear. Still, these results give important information about analytic solution sensitivity in the general range of values experienced in testing (e.g. shell thickness does not significantly

vary). The two input values which have wide ranges and derivatives which significantly change are r_0 and P . This can qualitatively be seen in Figure 4.6. Thus, data points for Table 4.6 and Table 4.7 are located at the rising section of the σ_t vs. P curve, as opposed to the flat section at the peak in σ_t (Figure 4.9). This prevents significantly underestimating sensitivity.

One of the advantages of NESSUS is the inclusion of a sensitivity analysis which is automatically incorporated into the results [24]. Shown in Figure 4.13 are sensitivity results from the 50% CDF (mean) output of the AMV+ method. Not surprisingly, they support the relative order of sensitivity shown in Table 4.6 and Table 4.7.

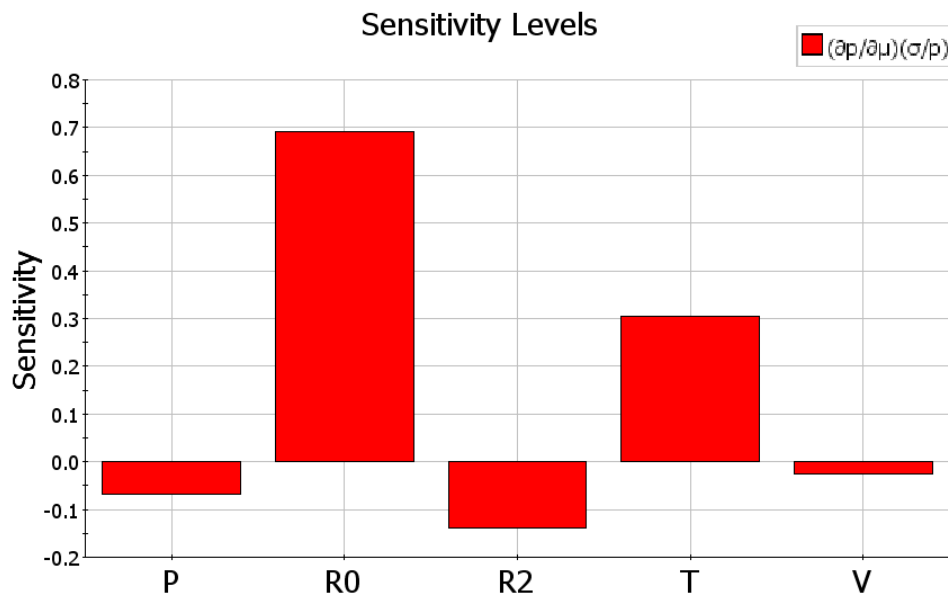


Figure 4.13: Analytic Solution Sensitivity Levels from AMV+ Method

The second most important input variables are shell geometry parameters, which is not surprising. Again, from all the sensitivity and importance results it is evident that r_0 & δr_0 have a greater impact on σ_t than any other input variable. Thus, it is safe to assume that divot asphericity also has a significant impact on test results. Therefore, experimental testing actions which can reduce divot asphericity and/or improve accuracy of divot measurements should be taken.

4.4.3 FEA Error and Sensitivity

The FEA model is a numerical “black box” when it comes to propagating errors using the delta method and it is too time consuming to perform a Monte Carlo simulation. Thus, AMV+ is the only method that can be used to estimate error and sensitivity in the FEA model. Shown in Figure 4.14 are the FEA sensitivity results evaluated at the mean.

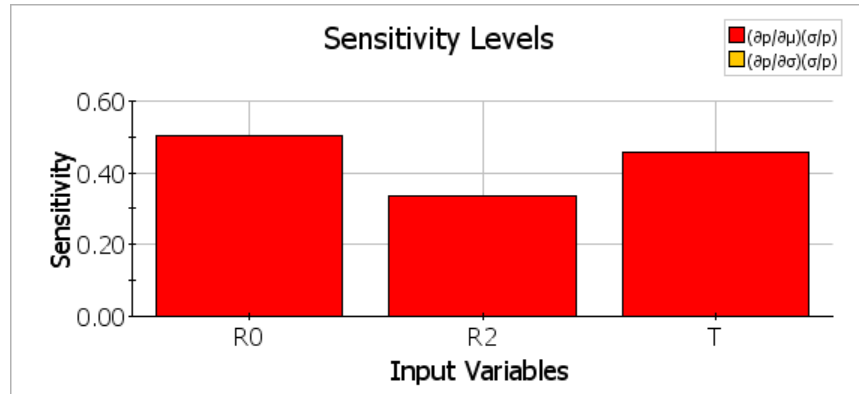


Figure 4.14: FEA Model Sensitivity Levels from AMV+ Method

It is very important to note that these results are much less reliable than the analytic solution. This is because changing one variable in the FEA model has an affect on other variables. For example, increasing the thickness in the shell increases the overall stiffness. In turn, the existing value for adjusting divot depth (C_{adj}) is no longer valid. Thus, increasing shell thickness also changes the volume of indenter material displaced by the shell. Additionally, increases in shell outside radius affect divot radius, making it not entirely independent. Thus, results which show a large effect from increasing thickness or outer radius may be correct, or they may be showing an effect from a secondary mechanism. Still, these results are included for thoroughness, regardless of concerns about their accuracy.

4.5 Discrete Empirical Data Points

All of the previous analysis reported herein has been performed on different theoretical data points based on “average” test articles. In this effort, the analysis has been significantly

developed and it is ready to be applied to discrete empirical data points obtained in lab testing.

4.5.1 Analytic Solution with Error Propagation

For visualization, linearly interpolated curves are included in the analysis. Shown in Figure 4.15 is r_0 vs. P and a power law curve for brass and nickel populations.

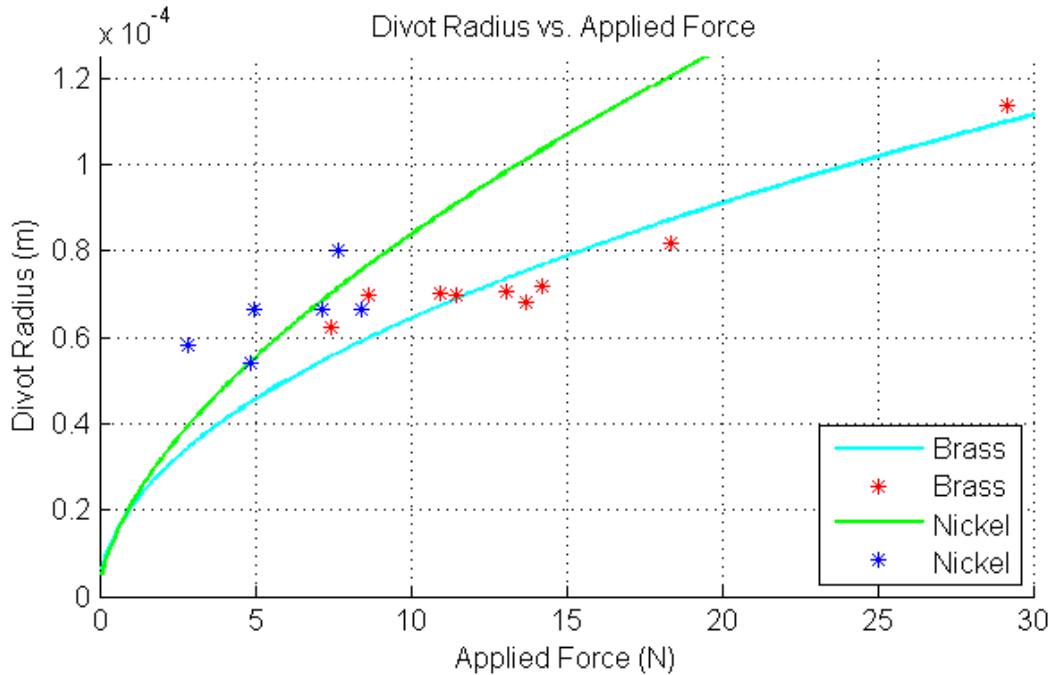


Figure 4.15: Results of Pseudo-Hardness Test on Crush Plate Material

Figure 4.15 shows several points at $r_0 \sim 70\mu m$ with a wide range of P . Thus, the crush test does not function as a consistent hardness test of the crush plate, presumably due to shell asphericity. Additionally, there isn't a curve which will accurately predict r_0 vs. P , thus the curve for σ_t vs. P (Figure 4.16) isn't expected to be an accurate predictor of empirical data points either. (Tabular Data: Table A.4)

From the results in Figure 4.15 and Figure 4.16, there is only one outlier: sample T011712-5 ($P = 29.17N$). Not only does P flag it as an outlier, but its qualitative location on the σ_t vs. P curve suggests a secondary failure mechanism. Thus, it will be removed from the population for any further calculations.

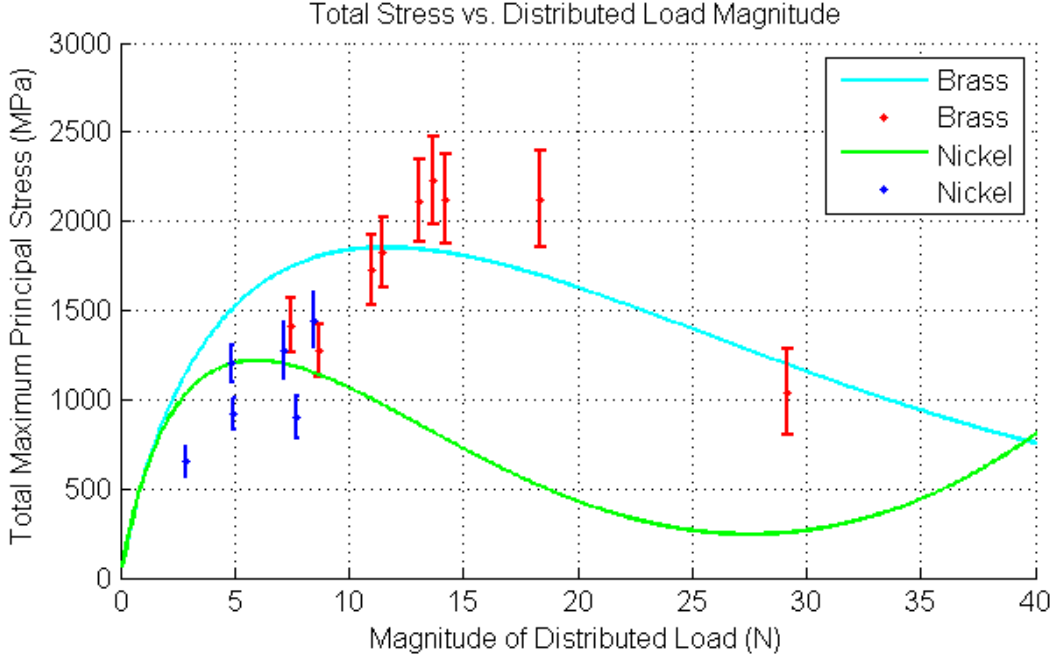


Figure 4.16: Analytic Solution with Error Bars for Empirical Data Points

From Figure 4.16 it is evident that most test articles fail on a rise in σ_t . Not only is this expected (as previously stated herein), but it also reinforces the notion that nearly all the articles are failing from the same primary failure mechanism. Looking only at the y-axis of Figure 4.16, it can be seen that σ_t has a wide spread. To quantify this, the data must be analyzed as a Weibull distribution. For preliminary analysis, the Weibull input data for mean divot and full shell size is shown in Table 4.8.

Table 4.8: Input Data to Preliminary Weibull Distribution

Material	N	$\bar{r}_0(\mu m)$	$\bar{R}_2(\mu m)$	$\bar{t}(\mu m)$	$S_E^L(m^2)$	$S_E^F(m^2)$
Brass	8	70.5	397	37.4	1.56E-08	1.63E-06
Nickel	6	65.3	405	37.2	1.34E-08	1.70E-06
Both	14	68.3	401	37.3	1.46E-08	1.66E-06

As previously described, there are two ways to determine Weibull distribution parameters: a linear curve fit of the log-log plot and the maximum likelihood method. Preliminary results

of both methods are shown in Table 4.9.

Table 4.9: Results From Preliminary Weibull Distribution

Material	Method	m	σ_0^L	σ_0^F
Brass	Linear Curve Fit	4.5	2028	719
	Max. Likelihood	7.2	1990	1039
Nickel	Linear Curve Fit	3.1	1199	253
	Max. Likelihood	4.7	1169	415
Both	Linear Curve Fit	2.8	1718	308
	Max. Likelihood	3.5	1692	434

As noted in previous publications, Table 4.9 shows the linear curve fit as the more conservative estimator of σ_0^F and thus it is more suitable for engineering purposes [5][17]. As expected, when the two populations are analyzed in the same distribution, the value of m decreases, indicating a wider spread. This value of m is lower than previously published results, suggesting that the large spread is created by differences in the crush plates, not the test articles [4]. This is possibly due to a difference in divot radius measurement accuracy for different crush plate materials. Regardless, the range of values for σ_0^F match previous published results shown in Table 2.2.

While this data can be used as a preliminary study, it is far from final. In particular, S_E^L was considered to represent the entire divot area being under stress σ_t . However, it was shown in Figure 4.12 and Table 4.3 that the stress profile under the divot varies significantly (i.e. up to $\sim 33\%$). Thus, after analyzing specific FEA stress profiles of actual test articles, a more accurate iterative method of calculating σ_0^F and m will be implemented.

4.5.2 FEA Model Solution for Supremum Principal Stress

The finalized FEA model was applied to the individual shells fractured by the brass indenter, but not the nickel. One input to the FEA model is a true stress vs. true plastic

strain curve for the indenter material. This curve was initially generated for the brass. After testing, it was qualitatively determined that nickel was a less suitable material. Thus, the costly and time consuming process of creating this curve for the nickel was not undertaken.

FEA model results are shown alongside the previously reported analytic solution results in Table 4.10 and Figure 4.17.

Table 4.10: Analytic Solution & FEA Model: Stress, Force, and Divot Size

SN	Method	σ_t & σ_{pS} (MPa)	P & F_R (P)	r_0 & r_d (μm)
T011712-7	Analytic	2230	13.68	68.0
	FEA	2379	14.63	69.7
T011712-8	Analytic	1274	8.67	69.8
	FEA	2278	15.94	70.9
T011712-9	Analytic	1727	10.96	70.0
	FEA	2434	15.11	70.7
T011712-10	Analytic	2120	18.37	81.8
	FEA	2473	20.05	82.4
T011712-11	Analytic	2124	14.21	71.9
	FEA	2440	15.99	73.2
T011712-12	Analytic	1414	7.44	62.2
	FEA	2316	12.71	65.0
T011712-13	Analytic	1827	11.49	69.7
	FEA	2415	15.22	70.7
T011712-14	Analytic	2113	13.05	70.4
	FEA	2512	14.90	70.6

Table 4.10 shows that empirical data points from different solution methods do not match as well as the linearly interpolated curves in Figure 4.9. This is a result of the difference between the FEA power law curve fit and the empirical data points for divot radius vs. force (Figure 4.8). This relationship is the same in the linearly interpolated curves. In Table 4.10, the analytic solution uses empirical values of both divot radius and force, but the FEA model creates its own force based on divot radius. Thus, there is a deviation between the solutions.

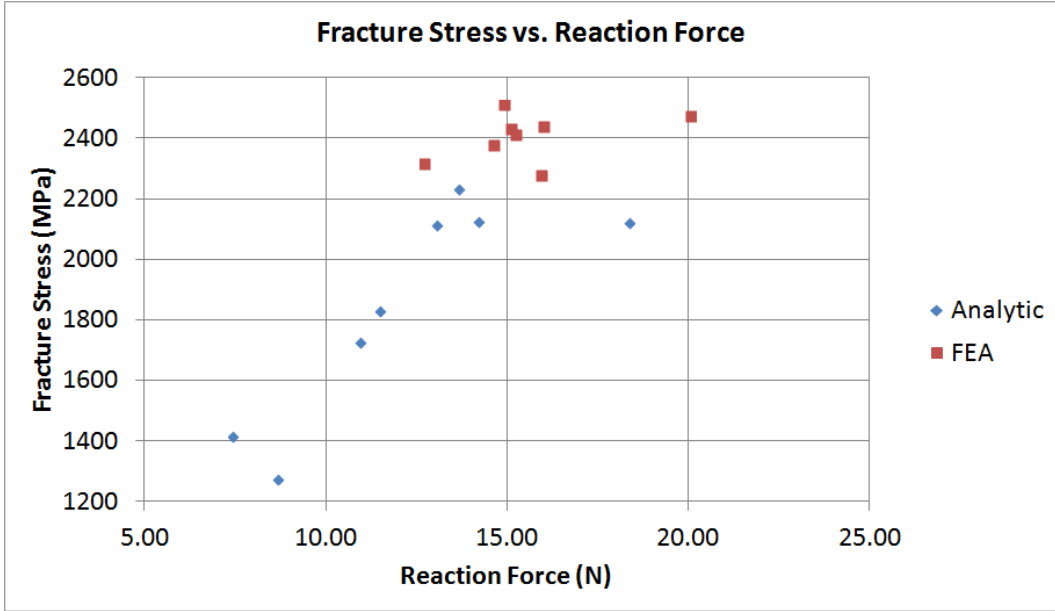


Figure 4.17: FEA Model σ_{pS} vs. F_R Empirical Data Points

The most extreme example is T011712-8, where a divot radius of $\sim 70\mu m$ creates the relatively small force of $8.67N$. This is likely a result of shell asphericity creating a shallow divot that does not displace much brass. The perfectly spherical shell in the FEA solution creates a divot with a similar radius that displaces more brass. Thus, the FEA solution shows a force of $15.94N$ and a much higher stress.

It can be qualitatively seen in Figure 4.17 that the FEA results have a much smaller spread. While it cannot be accurately quantified, this can be interpreted as the spread in the population when divot asphericity is removed. Thus, it is important to recognize that the m value in an analytic solution Weibull distribution is affected by variability in the ceramic and variability in asphericity. Regardless, the analytic solution produces lower values for fracture stress, making it the conservative result.

4.5.3 FEA Model Solution for Stress Profile

As previously stated, the preliminary Weibull distribution parameter for effective local surface area is the divot cross-sectional area. Using this value, the Weibull distribution takes the input of σ_t as the uniform stress over this entire area. It has been shown in Table 4.3 that

stress varies significantly in this region ($\sim 30\%$ for Table 4.11 test articles). Fortunately, FEA can produce stress profiles for each individual test article. These profiles were evaluated individually to find the radii at which stress is 90% of σ_{pS} . Figure 4.18 shows the profile within the entire divot radius and to the 90% maximum stress location. Tabular data is located in Table 4.11.

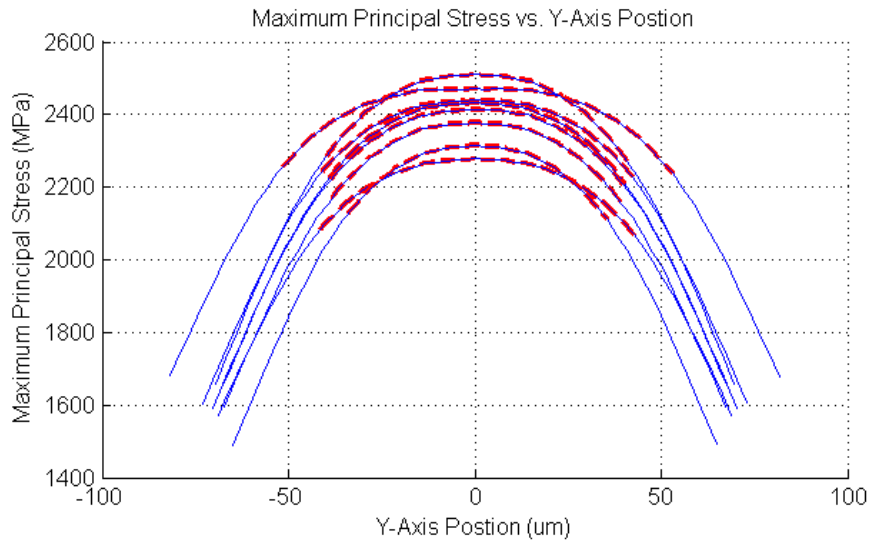


Figure 4.18: FEA Model Stress Profile on Inner Surface of SiC Shell

Table 4.11: FEA Model Stress Profile Numerical Data

Serial Number	σ_{pS}	$\sim (0.9)\sigma_{pS}$	$r_{90\%}(\mu m)$
T011712-7	2379	2154	39.4
T011712-8	2278	2069	42.6
T011712-9	2434	2212	40.0
T011712-10	2473	2240	52.9
T011712-11	2440	2228	42.3
T011712-12	2316	2112	35.3
T011712-13	2415	2208	39.6
T011712-14	2512	2272	40.7

These FEA profiles create new input data for a Weibull distribution. Thus, there will be two different distributions, one for the analytic solution and one for the FEA model. The values in Table 4.11 will be used for the FEA distribution. While the analytic solution is

able to use one value for S_E^L , the FEA model must be able to input multiple values of S_E^L into Weibull distribution calculations.

4.5.4 Iterative Weibull Distribution and Characteristic Strength

Regardless of whether fracture strength estimates are determined by the analytic solution or FEA, both sets of results must be analyzed in a Weibull distribution in order to determine the characteristic strength and Weibull modulus. In general, this is standard practice for determining fracture strength of ceramics [26]. Specific to this research, the iterative method described in Equations (3.32) & (3.33) was used.

Input data for the iterative method of determining Weibull distribution parameters is located in Table A.4 and Table 4.11 (analytic solution and FEA model, respectively). The results for characteristic strength and Weibull modulus for the full TRISO SiC shell are shown in Table 4.12.

Table 4.12: Results From Iterative Method Weibull Distribution

Material	Solution Method	m	σ_0^F
Brass	Analytic	4.1	653.5
	FEA	25.2	1954
Nickel	Analytic	2.9	228.7
Both	Analytic	2.5	255.8

Before discussing the results in Table 4.12, it must be understood that these numbers were generated from relatively small populations. For a more valid comparison, larger data sets must be used. Still, numerous observations can be made:

- The analytic solution results of the nickel crush plate data set are suspect.
 1. The Weibull modulus is less than published values, indicating something other than the SiC as the reason for high spread in the data [4].

2. The characteristic strength is on the extreme low end of the lowest range in previously published data [4].
- The analytic solution results of the total population appear to gravitate towards the suspect nickel values, not the brass values. This population is primarily for informational purposes and should not be used to draw steadfast conclusions.
 - The analytic solution results of the brass crush plate fall well within the overall range of previously published results.
 1. The Weibull modulus is in the range of numerous other published results, including the most recent diametrical compression tests [5][17].
 2. The characteristic strength is in the range of numerous other published results. It is out of the range of the most recent diametrical compression tests by only $\sim 0.6\%$, a deviation that is easily covered by any estimation of error in the test [5][17].
 - The FEA model results of the brass crush plate are highly suspect.
 1. The Weibull modulus is much higher than published research
 - Figure 4.17 shows low variability, which creates a large m value. This is most likely due to the lack of asphericity in the shell and the brass indenter Power Law curve which always maintains a close relationship between force and divot size.
 2. The characteristic strength is much higher than published research
 - Not only does the FEA produces higher fracture strengths, but the larger m value means there is less scaling, resulting in a larger σ_0^F .

Initially, the nickel crush plate was used in the hopes of finding a better alternative to the brass. The results contained herein show that it is not. It was also hoped that an FEA

solution would provide better numerical results. It has not done this. However, it has produced valuable results in terms of characterizing the test. The results of all the data sets indicate a potential issue which must be taken into consideration when evaluating results: divot asphericity.

4.5.5 Divot Size and Asphericity

As previously stated, nickel crush plate results are suspect due to values of m and σ_0^F which are outside previous published research. Additionally, divot radius has been shown to be the most influential factor in determining stress. Shown in Figure 4.19 are divots in brass (left) and nickel (right).

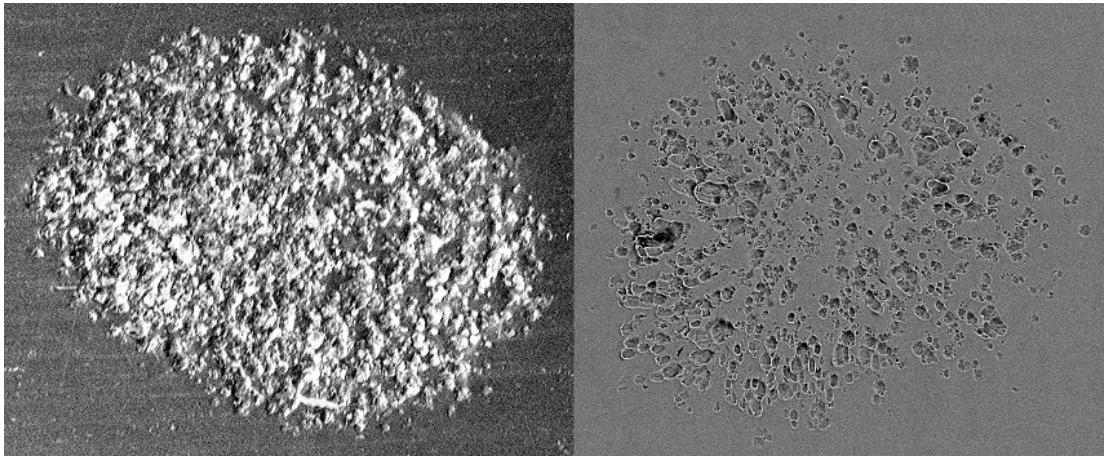


Figure 4.19: Typical Brass (left) and Nickel (right) Divot Marks under SEM

While the brass divot has an obvious border, the nickel does not. Thus, just by subjective judgment, the divot size in the nickel crush plate has more uncertainty. This is considered to be one of the major factors contributing to the low m value. With the qualitative assessment, the nickel analysis was halted and the full analysis is reserved for brass crush plate tests.

Equation (3.23) was applied to brass crush plate data points. Stress is plotted against these results and shown in Figure 4.20.

Visually, there is no correlation between σ_t and r_{0asp} . This is especially evident when viewing three different r_{0asp} values associated with $\sigma_t \sim 2100MPa$. However, the data set can be

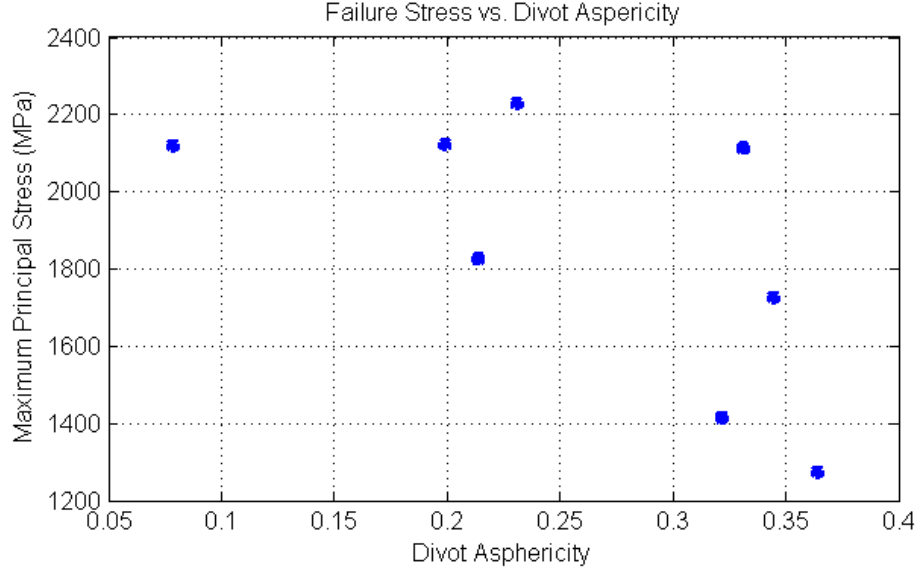


Figure 4.20: Stress (σ_t) vs. Dimensionless Divot Asphericity (r_{0asp})

broken into two sub sets: $r_{0asp} < 0.25$ and $r_{0asp} > 0.25$. The normal distribution parameters of these data sets are shown in Table 4.13.

Table 4.13: Fracture Strength for High and Low Asphericity Divot Sizes

Test Article Fracture Strength (MPa)		
	Mean	Std.Dev.
Total Population (8)	1854	358
Samples $r_{0asp} < 0.25$ (4)	2075	173
Samples $r_{0asp} > 0.25$ (4)	1632	373

When data points with $r_{0asp} > 0.25$ are removed, the standard deviation is reduced by more than half. While it cannot be stated that σ_t rises or falls with r_{0asp} , it can be stated that uncertainty in σ_t rises with r_{0asp} . Qualitatively, this reinforces the self-evident fact that the more the test deviates from the constraints of the analytic solution, the more uncertainty there is in the results. The same data sub-sets were also analyzed in the iterative method of determining Weibull distribution parameters. These results are located in Table 4.14.

Table 4.14: Fracture Strength for High and Low Asphericity Divot Sizes

Weibull Distribution Parameters		
	m	σ_0^F (MPa)
Total Population (8)	4.1	653
r0asp < 0.25 (4)	8.4	1264
r0asp > 0.25 (4)	3.3	438

The difference in m values in Table 4.14 (especially $m = 8.4$) confirms the same dynamics of uncertainty as Table 4.13. Quantitatively, there is now a range of values ($r_{0asp} > 0.25$) where data points can be judiciously removed.

It should also be noted that most samples with higher asphericity fracture at lower stresses. Removing them from the population results in a higher m and σ_0^F . Ultimately, these results suggest that the diametrical compression test is inherently conservative, both in overestimating uncertainty in the population and underestimating the strength of the shell. High asphericity tests could be removed to create more accurate results. However, due to the nuclear safety nature of this research, including high asphericity samples and producing conservative values of m and σ_0^F creates a “warm and fuzzy” rationale.

4.5.6 Multi-Method Conservative Weibull Distribution

Taking into consideration all of the previous results, a conservative yet reasonable solution can be pursued by using select results from different methods. The following steps illustrate the conservative nature of the process:

1. The brass crush plate population was selected to provide reliable empirical data.
2. Using analytic results, one data point was removed as an outlier. This shell fractured at an extremely high load, most likely due to a secondary failure mechanism. If it was not a true outlier, removing it from the population effectively removes the strongest test article. This is either neutral or conservative.

3. Test articles which produced high divot asphericity were not removed from the population. While these samples may decrease accuracy, they also decrease σ_f and m , both of which reduce the characteristic strength of the full shell (σ_0^F). This is a conservative inaction.
4. Fracture strength of each test article (σ_f) was determined using the analytic solution instead of the FEA model because the analytic solution produces consistently lower fracture strengths (Table 4.10). This is a conservative action.
5. The local area under stress (S_E^L) was determined using the $r_{90\%}$ value from the FEA model stress profiles (Table 4.11). Compared to divot radius, this is a more accurate and conservative representation of surface area under high stress.
6. The final Weibull distribution parameters were determined through the linear curve fit method. Multiple researchers have found this to be conservative.

The final results of this amalgamated method are: $\sigma_0^F = 487MPa$, $m = 4.0$. These results are well within the range of other published results for isolated SiC shells of TRISO coatings [4].

CHAPTER 5

CONCLUSIONS

There are two engineering philosophies that can direct decision making in the testing and analysis of TRISO SiC Shells:

1. All reasonable efforts must be made to increase the accuracy of testing and analysis results. Then, a gratuitous safety factor is applied to these results.
2. Conservative estimations are made at every intermediate step in testing and analysis efforts. Then, a reasonable safety factor is applied.

Due to inherent variability in shell geometry, which causes issues such as divot asphericity, it was not practical to pursue item #1 listed above. Instead, there were numerous actions taken to produce extremely conservative results. However, it is important to understand that sacrifices in accuracy were made.

As part of this research, substantial efforts were made to characterize the test and understand the overall mechanics. From these efforts, there are numerous conclusions that can be passed on to future researchers:

1. Diametrical compression tests produce stress concentrations directly under the contact area. Thus, these are highly localized tests and conditions outside of this local area have little effect on the results.
2. In order to create a failure under a biaxial stress condition, the crush plate material must be carefully chosen so that the resulting stress profile on the inner shell surface has a single maximum at the apex. This is demonstrated in the stress profile plot (Figure 4.10) which shows that larger divot sizes result in maximum stresses away from the apex.

3. The crush plate material must be properly modeled in FEA and stress profile solutions must be made for the range of forces and divot sizes experienced in testing. This model is the only way to verify that the resulting stress profile at fracture has a single maximum at the apex.
4. In scaling Weibull distribution results from the local area to the full shell, the power of $(1/m)$ shown in (3.30) prevents the solution of σ_0^F from being hyper-sensitive to small local areas. Thus, the difference in local surface area is not a significant detractor to using the diametrical compression test over the internal pressurization test.
5. Even with reduced scaling in the Weibull distribution, estimating the local surface area by the divot radius is not accurate and counter-productive to conservative efforts. Therefore, local surface area should be estimated using a smaller radius, such as the $r_{90\%}$ described herein.
6. The resulting fracture stress is most sensitive to changes in divot radius. Hence, refinement efforts can be valuably spent on improving methodology for accurately quantifying divot radius or distribution of pressure on the contact surface of the shell. (Fracture stress is secondarily sensitive to changes in shell geometry: thickness and outside radius.)
7. Shell asphericity and the resulting divot asphericity introduces significant variability to the test. This is best demonstrated by the force vs. divot radius plot (Figure 4.15) which shows the same divot radius being produced by a wide range of forces. Thus, not all variability in results can be attributed to flaw distribution in the ceramic.
8. The major limiting factor in test result precision is the inherent asphericity in the shell. Hence, there is a point of depreciating returns where improvements in measurement precision will no longer improve precision in the final results.

9. Due to the inherent uncertainty in shell geometry, the refinement of this test could be a never-ending pursuit. Therefore, it is prudent to finish test methodology development at some time and focus strictly on testing shell populations.

Ultimately, the methodology described herein produces acceptably conservative results for characteristic strength and Weibull modulus. This methodology also represents a value added step forward in the overall conduction of diametrical compression tests on isolated TRISO coating SiC shells.

Even when considering this progress, there is still room for future improvements as an extension of research reported herein. There are several recommendations which can be made for potential future work:

1. Currently, there is no way to separate the variability in results by cause. The two major suspected causes are: inherent variability of flaws in a ceramic and variability introduced by shell asphericity. Future work can quantify the contributions of each cause (and currently unrecognized potential causes).
2. The current 3D FEA models with no shell asphericity show a lower variability in results. Introducing asphericity into the models can help distinguish causes of variability. This can be done by using x-ray tomography to import shapes of actual test articles into the 3D FEA model.
3. For tests that ignore asphericity, identical tests can be run using the 3D FEA model and the ORNL 2D FEA models. If there is no significant difference in results, the 2D models can be used with smaller element discretization for the same computational costs, thus improving accuracy.

Therefore, future work can apply current methods to larger sample populations, or further the continuous improvement process of testing and analysis methodology.

REFERENCES CITED

- [1] Idaho National Laboratory. Next Generation Nuclear Plant Project 2009 Status Report, 2009.
- [2] Idaho National Laboratory. Summary for the Next Generation Nuclear Plant Project in Review, 2010.
- [3] US Department of Energy. Next generation nuclear plant licensing strategy, a report to congress, August 2008.
- [4] Lance L. Snead, Takashi Nozawa, Yutai Katoh, Thak-Sang Byun, Sosuke Kondo, and David A. Petti. Handbook of sic properties for fuel performance modeling. *Journal of Nuclear Materials*, 371(13):329 – 377, 2007.
- [5] Thak Sang Byun, Jin Weon Kim, Ivan Dunbar, and John D. Hunn. Fracture stress data for sic layers in triso-coated fuel particles. Technical Report ORNL/TM-2008/167, Oak Ridge National Laboratory, September 2008.
- [6] MatWeb LLC. Cartridge brass, uns c26000 (260 brass), os070 temper flat products, Dec. 20012. URL http://www.matweb.com/search/datasheet_print.aspx?matguid=83677ae92338456da4d4afe8fe4b815c5.
- [7] K. Bongartz, E. Gyarmati, H. Nickel, H. Schuster, and W. Winter. Measurement of young’s modulus and fracture stress on htr particle coatings by the brittle ring test. *Journal of Nuclear Materials*, 45(3):261 – 264, 1972.
- [8] S. Timoshenko. *Strength of Materials, Part 2: Advanced Theory and Problems*. D. Van Nostrand Company, second edition, 1956.
- [9] K. Bongartz, E. Gyarmati, H. Schuster, and K. Tuber. The brittle ring test: A method for measuring strength and young’s modulus on coatings of htr fuel particles. *Journal of Nuclear Materials*, 62(23):123 – 137, 1976.
- [10] Kazuo Minato, Kousaku Fukuda, and Katsuichi Ikawa. Strength of silicon-carbide coating layers of fuel particles for high temperature gas-cooled reactors. *Journal of Nuclear Science and Technology*, 19(1):69–77, 1982.
- [11] S.J. Xu, J.G. Zhou, B. Yang, and B.Z. Zhang. Effect of deposition temperature on the properties of pyrolytic sic. *Journal of Nuclear Materials*, 224(1):12 – 16, 1995.

- [12] K.E. Gilchrist and J.E. Brocklehurst. A technique for measuring the strength of high temperature reactor fuel particle coatings. *Journal of Nuclear Materials*, 43(3):347 – 350, 1972.
- [13] Seong-Gu Hong, Thak-Sang Byun, Richard A. Lowden, Lance L. Snead, and Yutai Katoh. Evaluation of the fracture strength for silicon carbide layers in the tri-isotropic-coated fuel particle. *Journal of the American Ceramic Society*, 90(1):184–191, 2007.
- [14] T.S Byun, S.G. Hong, L.L Snead, and Y.Katoh. Influence of specimen type and loading configuration on the fracture strength of sic layer in coated particle fuel. In *Proceedings of the 30th International Conference on advanced ceramics and composites*. The American Ceramic Society, Wiley, 2006.
- [15] A. G. Evans, C. Padgett, and R. W. Davidge. Strength of pyrolytic sic coatings of fuel particles for high-temperature gas-cooled reactors. *Journal of the American Ceramic Society*, 56(1):36–41, 1973.
- [16] A. Briggs, R.W. Davidge, C. Padgett, and S. Quickenden. Crushing behaviour of high temperature reactor coated fuel particles. *Journal of Nuclear Materials*, 61(3):233 – 242, 1976.
- [17] Thak Sang Byun, John D. Hunn, James H. Miller, Lance L. Snead, and Jin Weon Kim. Evaluation of fracture stress for the sic layer of triso-coated fuel particles using a modified crush test method. *International Journal of Applied Ceramic Technology*, 7 (3):327–337, 2010.
- [18] Andrew K. Kercher, John D. Hunn, Jeffery R. Price, and Pete Pappano. Automated optical microscopy of coated particle fuel. *Journal of Nuclear Materials*, 380(13):76 – 84, 2008.
- [19] Wikimedia Foundation Inc. Sagitta (geometry), 2012. URL [http://en.wikipedia.org/wiki/Sagitta_\(geometry\)](http://en.wikipedia.org/wiki/Sagitta_(geometry)).
- [20] Warren C Young and Richard Gordon Budynas. *Roark’s formulas for stress and strain; 7th ed.* McGraw-Hill, New York, NY, 2002.
- [21] E. Reissner. Stresses and small displacements of shallow spherical shells, ii. *Journal of Math and Physics*, 25(4):233 – 242, 1947.
- [22] *Mathematical Statistics and Data Analysis*. Duxbury Press, 3 edition, 2001. ISBN 0534399428. URL <http://www.worldcat.org/isbn/0534399428>.
- [23] J.H. Hollomon. *Trans. Metall. Soc. AIME*, 162:268 – 290, 1945.

- [24] *NESSUS Theoretical Manual*. Southwest Research Institute, june 9, 2010 edition, 2010.
- [25] David Riha, Barron Bichon, John McFarland, and Simeon Fitch. *NESSUS Users' Manual*. Southwest Research Institute, september 10, 2010 edition, 2010.
- [26] ASTM International West Conshohocken, PA. Standard practice for reporting uniaxial strength data and estimating weibull distribution parameters for advanced ceramics, 2007. URL <http://www.astm.org>. DOI: 10.1520/C1239-07.
- [27] Wikimedia Foundation Inc. Weibull distribution, 2012. URL http://en.wikipedia.org/wiki/Weibull_distribution.

APPENDIX - SELECT ANALYSIS RESULTS IN TABULAR FORM

Table A.1: FEA Intermediate Convergence Studies

Test	SiC Shell				Brass Indenter				Results	
	Circ	Rad	Thck	Bias	Circ	Rad	Thck	Bias	MaxP	RF
c1-01	5	5	5	5	6	5	5	5	878	6.51
c1-02	7	5	5	5	6	5	5	5	952	6.39
c1-03	7	5	7	5	6	5	5	5	1049	6.51
c1-04	7	7	7	5	6	5	5	5	1047	6.50
c1-05	7	7	7	7	6	5	5	5	1048	6.49
c1-06	10	7	7	7	6	5	5	5	1050	6.70
c1-07	10	7	10	7	6	5	5	5	1144	6.72
c1-08	10	10	10	7	6	5	5	5	1143	6.71
c1-09	10	10	10	10	6	5	5	5	1144	6.71
c1-10	15	10	10	10	6	5	5	5	1131	6.79
c1-11	15	10	15	10	6	5	5	5	1237	6.81
c1-12	15	15	15	10	6	5	5	5	1237	6.80
c1-13	15	15	15	15	6	5	5	5	1238	6.80
c1-14	20	15	15	15	6	5	5	5	1205	6.84
c1-15	20	15	20	15	6	5	5	5	1420	6.84
c1-16	20	20	20	15	6	5	5	5	1420	6.84
c1-17	20	20	20	20	6	5	5	5	1420	6.84
c1-18	25	20	20	20	6	5	5	5	1258	6.69
c1-19	25	20	25	20	6	5	5	5	1281	6.70
c1-20	25	25	25	20	6	5	5	5	1281	6.70
c1-21	25	25	25	25	6	5	5	5	1281	6.70
c1-22	30	25	25	25	6	5	5	5	1260	6.89
c1-23	30	25	30	25	6	5	5	5	1276	6.89
c1-24	30	30	30	25	6	5	5	5	1275	6.89
c2-01	15	10	15	10	6	5	5	5	1304	6.80
c2-02	15	10	15	10	8	5	5	5	1293	6.83
c2-03	15	10	15	10	8	5	8	5	1291	6.80
c2-04	15	10	15	10	8	8	8	5	1289	6.80
c2-05	15	10	15	10	8	8	8	8	1285	6.84
c2-06	15	10	15	10	10	8	8	8	1404	6.36
c2-07	15	10	15	10	10	8	10	8	1266	7.04
c2-08	15	10	15	10	10	10	10	8	1267	7.03
c2-09	15	10	15	10	10	10	10	10	1267	7.03
c2-10	15	10	15	10	16	10	10	10	1310	6.78
c2-11	15	10	15	10	16	10	15	10	1282	6.95
c2-12	15	10	15	10	16	15	15	10	1282	6.94
c2-13	15	10	15	10	16	15	15	15	1282	6.94
c2-14	15	10	15	10	20	15	15	15	1269	7.05
c2-15	15	10	15	10	20	15	20	15	1250	7.21
c2-16	15	10	15	10	20	20	20	15	1250	7.21

Table A.2: FEA Main Convergence Study

			SiC Shell						
Article	Run	Rzone	R2	t	Circ	Rad	Thck	Bias	AR
BrAv01	01	150	398	37.1	4	5	3	10	0.5
BrAv01	02	150	398	37.1	6	5	5	10	0.4
BrAv01	03	150	398	37.1	10	5	10	10	0.3
BrAv01	04	150	398	37.1	16	5	15	10	0.4
BrAv01	05	150	398	37.1	20	5	20	10	0.3
BrAv01	06	150	398	37.1	26	5	25	10	0.4
BrAv01	07	150	398	37.1	30	5	30	10	0.3
BrAv01	08	150	398	37.1	36	5	35	10	0.4
BrAv01	09	150	398	37.1	40	5	40	10	0.3
			Brass Indenter						
Article	Run	Rzone	R	t	Circ	Rad	Thck	Bias	AR
BrAv01	01	150	800	400	20	10	40	10	1.9
BrAv01	02	150	800	400	20	10	40	10	1.9
BrAv01	03	150	800	400	20	10	40	10	1.9
BrAv01	04	150	800	400	20	10	40	10	1.9
BrAv01	05	150	800	400	20	10	40	10	1.9
BrAv01	06	150	800	400	26	10	50	10	2.0
BrAv01	07	150	800	400	30	10	60	10	1.9
BrAv01	08	150	800	400	36	10	70	10	1.9
BrAv01	09	150	800	400	40	10	80	10	1.9
			Results						
						Wall Time		Change	
Article	Run		MaxP	RF	Frm	(s)	(hr)	MaxP	RF
BrAv01	01		1305	13.59		6354	1.8		
BrAv01	02		1811	13.86		6105	1.7	38.80%	1.95%
BrAv01	03		2190	14.05		6993	1.9	20.91%	1.43%
BrAv01	04		2339	14.05		8344	2.3	6.80%	0.03%
BrAv01	05		2422	14.06		9174	2.5	3.54%	0.08%
BrAv01	06		2455	14.16		41317	11.5	1.39%	0.69%
BrAv01	07		2490	14.13		96889	26.9	1.41%	0.21%
BrAv01	08								
BrAv01	09								

Table A.3: FEA Model Linearly Interpolated Solution

FEA Model Input Data			
R2			396
t			37.3
Cadj			0
Element Configuration			“05”
FEA Group Designator			“af2”
Materials File	mat_Logan_Brass_Quad_r1.csv		
Results			
r_{dp}	F_R	r_d	σ_{pS}
30	1.429	22.5	769.1
40	2.935	30.1	1276.8
50	5.092	37.7	1726.8
60	7.692	52.9	2086.6
70	11.31	60.6	2307.3
80	15.628	72.1	2399.6
90	20.761	83.7	2345.5
100	26.816	91.8	2157.1
110	33.96	107	1974.9
120	41.875	119	2010.5
130	48.754	131	2276.9
140	54.4	147	2567.1

Table A.4: Analytic Solution with Error for Empirical Data

	Test Article	σ_t	$\delta\sigma_t$	$\sigma_t - \delta\sigma_t$	$\sigma_t + \delta\sigma_t$	r_0
Brass	'T011712-7'	2230	244	1986	2474	68.0
	'T011712-8'	1274	146	1128	1420	69.8
	'T011712-9'	1727	197	1530	1924	70.0
	'T011712-10'	2120	270	1850	2391	81.8
	'T011712-11'	2124	254	1870	2378	71.9
	'T011712-12'	1414	150	1264	1565	62.2
	'T011712-13'	1827	196	1631	2024	69.7
	'T011712-14'	2113	230	1884	2343	70.4
	'T062812-2'	922	88	834	1010	66.6
Nickel	'T062812-3'	904	117	787	1021	79.9
	'T062812-5'	1203	104	1099	1307	54.2
	'T062812-11'	652	84	568	736	58.1
	'T062812-12'	1272	158	1115	1430	66.6
	'T062812-16'	1444	152	1291	1596	66.3

Table A.5: Empirical Input Data (with Height-Corrected Geometry)

SN	$F(N)$	r_{0min}	r_{0av} (μm)	r_{0max}	ν	t (μm)	δt (μm)	R_{min}	R_{av} (μm)	R_{max}
T011712-5	29.17	104.8	113.5	122.2	0.21	37.5	1.6	389	398	407
T011712-7	13.68	60.1	68.0	75.8	0.21	38.0	1.7	389	397	406
T011712-8	8.67	57.7	69.8	83.1	0.21	38.1	1.7	370	378	386
T011712-9	10.96	59.0	70.0	83.1	0.21	37.6	1.8	393	402	411
T011712-10	18.37	79.0	81.8	85.4	0.21	37.3	0.8	407	413	419
T011712-11	14.21	65.3	71.9	79.6	0.21	37.0	1.9	388	397	406
T011712-12	7.44	53.9	62.2	73.9	0.21	37.3	1.8	374	384	393
T011712-13	11.49	62.9	69.7	77.8	0.21	37.2	1.2	393	398	404
T011712-14	13.05	59.6	70.4	82.9	0.21	36.7	1.0	398	408	418
T062812-2	4.97	61.2	66.6	72.6	0.21	37.2	0.8	420	427	434
T062812-3	7.70	70.8	79.9	89.0	0.21	39.6	2.6	409	416	424
T062812-5	4.85	47.2	54.2	61.2	0.21	37.1	1.3	396	404	412
T062812-11	2.84	48.6	58.1	67.9	0.21	35.3	2.9	380	388	397
T062812-12	7.13	59.3	66.6	74.6	0.21	35.4	2.5	382	388	395
T062812-16	8.44	58.6	66.3	73.5	0.21	38.8	1.8	399	407	414